Materials Science & Engineering A 889 (2024) 145793

Contents lists available at ScienceDirect

Materials Science & Engineering A

journal homepage: www.elsevier.com/locate/msea

The role of parent austenite grain size on the variant selection and intervariant boundary network in a lath martensitic steel

Ahmad Mirzaei [a], Peter D. Hodgson [a], Xiang Ma [b], Vanessa K. Peterson [c], Ehsan Farabi [a,d], Gregory S. Rohrer [e], Hossein Beladi [a,*]

[a] Institute for Frontier Materials, Deakin University, Geelong, Victoria, 3216, Australia
[b] SINTEF Industry, P.O.B 124, Blindern, 0314, Oslo, Norway
[c] Australian Centre for Neutron Scattering, Australian Nuclear Science and Technology Organisation, Lucas Heights, New South Wales, 2234, Australia
[d] School of Materials Science and Engineering, University of New South Wales, Sydney, New South Wales, 2052, Australia
[e] Department of Materials Science and Engineering, Carnegie Mellon University, Pittsburgh, PA, 15213-3890, USA

ARTICLE INFO

Keywords:
Lath martensite
Intervariant boundary network
Parent austenite grain refinement
In situ neutron diffraction
Variant selection
Impact toughness

ABSTRACT

This study investigated the influence of parent austenite grain refinement on the intervariant boundary network (population and connectivity) in a lath martensitic steel. Parent austenite grain refinement revealed a progressive reduction in the fraction of the 60° misorientation boundaries in martensite, which was linked to a decrease in the 60°/[110] intervariant boundary population. The phenomenological theory of martensite crystallography demonstrated that the variant selection mechanism altered from the 3-variant clustering ($V_1V_3V_5$) in the coarse parent austenite towards the 4-variant clustering ($V_1V_2V_3V_4$) in the fine parent austenite grain, due to the change in the lattice parameter of the parent and daughter phase in which the martensite transformation occurs, as measured using *in situ* neutron diffraction. The change in the variant clustering arrangement with the parent austenite grain refinement led to a progressive promotion of 60°/[111] and 10.5°/[011] intervariant boundaries at the expense of 60°/[110] martensite intervariant boundaries. Subsequently, the connectivity of low energy {110} tilt intervariant boundaries gradually increased through the refinement of parent austenite grain size, eventually reducing the high energy {110} twist boundary connectivity. This change improved the impact toughness of martensite produced from the fine-grained austenite as the weak connectivity of high energy boundaries delays the coalescence of voids, promoting ductile fracture.

1. Introduction

The grain boundary is an active structural element, which plays an important role in the chemical, mechanical, and functional properties of polycrystalline materials, including corrosion resistance [1,2], intergranular cracking [2,3], slipping [2,4], and segregation of impurities such as hydrogen [5,6]. The design and control of the grain boundary in the microstructure, which is a concept of grain boundary engineering (GBE), has led to improved materials properties through the replacement of high energy boundaries with boundaries having a low energy configuration such as Σ3 grain boundaries found in face centred cubic (FCC) materials [7–11]. Iterative recrystallisation is the most common approach to manipulate the grain boundary network in austenitic FCC materials [7,12]. However, this approach cannot be utilised for materials undergoing phase transformation (e.g., steel), since the high temperature parent microstructure (e.g., grain boundary network) is replaced through phase transformation during cooling.

Studies have demonstrated that the characteristics of the parent austenite (i.e., composition [13] and deformation state [14]), along with cooling rate (i.e., the phase transformation mechanism), significantly influence the boundary network of the transformed products (i.e., ferrite, martensite and bainite) in low carbon low alloy steels [14–19]. The high temperature austenite in steel can undergo different phase transformation mechanisms (i.e., diffusion versus shear) depending on the cooling rate [14,15,18]. The martensitic shear transformation induces a distinct boundary network compared with the ferritic diffusional transformation [14,16,18]. For instance, the boundary with 60°/[111] misorientation in ferritic microstructure terminates at {112} planes with a low energy configuration, with mostly {110} planes in martensite. The latter is closely related to the crystallographic constraint associated with

* Corresponding author.
E-mail address: hossein.beladi@deakin.edu.au (H. Beladi).

https://doi.org/10.1016/j.msea.2023.145793
Received 16 August 2023; Received in revised form 25 September 2023; Accepted 9 October 2023
Available online 10 October 2023

the martensite displacive transformation rather than the promotion of low energy boundary arrangements that occurs during grain growth [14,18].

The change in steel composition alters the onset temperature of the martensite transformation M_s, which stimulates the formation of specific variant arrangement/s to accommodate the strain associated with the martensitic transformation [13,20]. This ultimately leads to the promotion of specific boundaries in martensite. The addition of Mn to steel, for example, reduces M_s, encouraging specific intervariant boundaries (e.g., 60°/[111]) due to local variant selection, altering the boundary network characteristics (i.e., population and connectivity) [13].

The deformation of the parent austenite not only reduces the start and finish temperature for the martensite transformation (M_s and M_f, respectively), it also importantly introduces a dislocation substructure within the parent austenite grains prior to the martensitic transformation [14,21]. The latter leads to the formation of specific variant/s whose habit planes {011}α' are closely parallel to the primary slip plane {111}γ and/or the secondary slip plane {1–11}γ [22,23]. The interaction of these variants stimulates the formation of specific boundaries (e.g., 60°/[111]), altering the boundary network in the martensitic steel [14].

Similar to chemical composition and pre-strained austenite condition, parent austenite grain refinement also reduces the martensite transformation temperature range (M_s - M_f) due to the restriction in both the number of variants nucleated within a parent austenite grain and their growth during the martensitic transformation [24–26]. It is, however, not clear whether the grain size also leads to a change in the characteristics of the martensite boundary network. Therefore, the current study aims to investigate the influence of the parent austenite grain size on the boundary network of a lath martensite. In this regard, the experimental material was exposed to cyclic heat treatment to refine the parent austenite grain prior to the martensitic transformation. The resulting grain boundary network was characterised by five-parameter grain boundary analysis and homology metrics approaches to measure the connectivity of different martensite intervariant boundaries. The result was interpreted using phenomenological theory of martensite crystallography (PTMC) to disclose the mechanism of variant selection due to the austenite grain refinement and its influence on the martensite boundary network, and consequently material performance (i.e., toughness).

2. Experimental procedure

The experimental material with a chemical composition of 0.043 C, 1.68 Mn, 0.2 Si, 0.017 Ti, 0.021 Nb, and 0.002 B wt.%, was received in the form of slab having a thickness of 40 mm. A multi-pass hot rolling process at the elevated temperature range of 1000–1200 °C was applied to the as-received slab to obtain a plate with a thickness of 12 mm.

Dilatometric measurement: To determine the critical transformation temperature, a DIL805A/D dilatometer equipped with an induction coil and extensometer was used. The cylindrical dilatometry samples were machined directly from the hot rolled slab with a length (10 mm) to diameter (4 mm) ratio of 2.5 in accordance with ASTM A1033-04 [27]. The samples were reheated to 1150 °C using an induction furnace in a vacuum chamber. The temperature was controlled by a K-type thermocouple spot-welded on the surface in the mid-length of the cylindrical sample. The cylindrical sample was clamped between two quartz push rods. The change in the length of sample and the push rods was measured during heating and cooling schedules using a linear variable displacement transducer. The length change in the sample stems from its thermal expansion or contraction upon heating and cooling, respectively. The cylindrical dilatometry samples were reheated at different heating rates (i.e., 1, 5, 10, 20, and 50 °C/s) to a temperature of 1150 °C and then held for 5 min. Afterwards, the samples were immediately cooled down to ambient temperature using a flow of Ar gas.

Thermal cycling heat treatment: Cyclic heat treatment was conducted using an induction furnace equipped with water quench facilities. The sample consisted of three parts: a two-part sample holder and a rectangular specimen (Fig. 1a–c). The holders had a 20 mm diameter and 54 mm length with a rectangular groove (i.e., 15 mm depth, 10.5 mm width, and 17 mm length) to position the rectangular specimen. A 3 mm hole was drilled throughout the length of the sample holder to position a thermocouple for monitoring the temperature (Fig. 1a and b). The rectangular samples with a dimension of $10 \times 10 \times 55$ mm^3 were machined along the hot rolling direction. A 3 mm diameter hole with a depth of 15 mm was also drilled from both ends of the rectangular sample, which were aligned with the shoulder holes to position the thermocouples and monitor the temperature throughout the test (Fig. 1a–c). The position of induction coil was adjusted so that the temperature difference between two ends of sample was kept within 10 °C (Fig. 1d). During the test, the sample was covered in a quartz tube filled with a positive pressure of Ar gas to prevent oxidation and decarburization. To monitor the evolution of the austenite grain size, the sample was water-quenched immediately (i.e., within 0.2 s) after each reheating cycle.

The thermal cycling process consisted of reheating the steel to single-phase austenite regime followed by water-quenching. The first cycle involved reheating the steel to 1000 °C at a rate of 20 °C/s and holding isothermally for 180 s. The sample was then water-quenched (W.Q.) immediately to obtain a fully lath martensitic microstructure. Some samples underwent further thermal cycling to investigate the effect on the parent austenite grain size. Thermal cycles 2 through 10 were similar, where the steel was reheated to 925 °C (just above the Ac_3 transformation temperature, i.e., 900 °C) at a rate of 20 °C/s and then held isothermally for 5 s followed by water-quenching. Afterwards, the austenite grain size was measured.

Charpy impact test: Impact tests were carried out on two martensitic specimens produced from coarse (i.e., ~84 μm) and fine (i.e., ~3 μm) parent austenite grains at room temperature using an Instron MPX pendulum impact machine. The standard Charpy U-notch specimens had a dimension of 10 mm × 10 mm × 55 mm (Fig. 1e). The U-notch was made by a wire-cut machine in the rolling direction - transverse direction (RD-TD) plane towards the normal direction (ND) with respect to the original hot-rolled plate. The test was repeated three times for each condition and the average value reported.

EBSD analysis: Microstructural characterisation was performed using electron backscatter diffraction (EBSD). The samples for EBSD were cut from the heat-treated specimens along the RD-ND plane. They were then mounted with the RD-ND plane parallel to the mount surface. Afterwards, standard mechanical grinding and polishing was carried out on the EBSD samples followed by final polishing with a colloidal silica slurry to obtain a mirror-like surface. EBSD measurements were performed using fully equipped FEI Quanta 3D scanning electron microscope. Data collection was carried out at an operating voltage of 20 kV, beam current of 4 nA, working distance of ~11 mm, and a step size of 0.15 μm. Multiple EBSD maps having an area of 120×120 μm^2 were acquired using a hexagonal grid. The raw EBSD maps had several processing steps before boundary segments were extracted using the TSL OIM analysis V8 software. The first processing step included grain dilation performed iteratively with a 5° tolerance angle and minimum grain size of 5 pixels. Subsequently, a single average orientation was assigned to each individual grain with a tolerance angle of 5°. Afterwards, grain boundaries with discrete steps from the orientation grid were smoothed using a boundary deviation limit of 2 pixels (i.e., 2×0.15 μm = 0.3 μm) to collect boundary line segments for grain boundary characterization using a five-parameter analysis approach [16]. On average, more than 50,000 boundary line segments were collected at each thermal cycle condition. The parent austenite grain reconstruction was also performed using TSL OIM V8 software, considering the Kurdjumov-Sachs orientation relationship (K–S OR).

In situ neutron diffraction: In situ neutron diffraction experiments were performed using the high intensity neutron powder diffractometer,

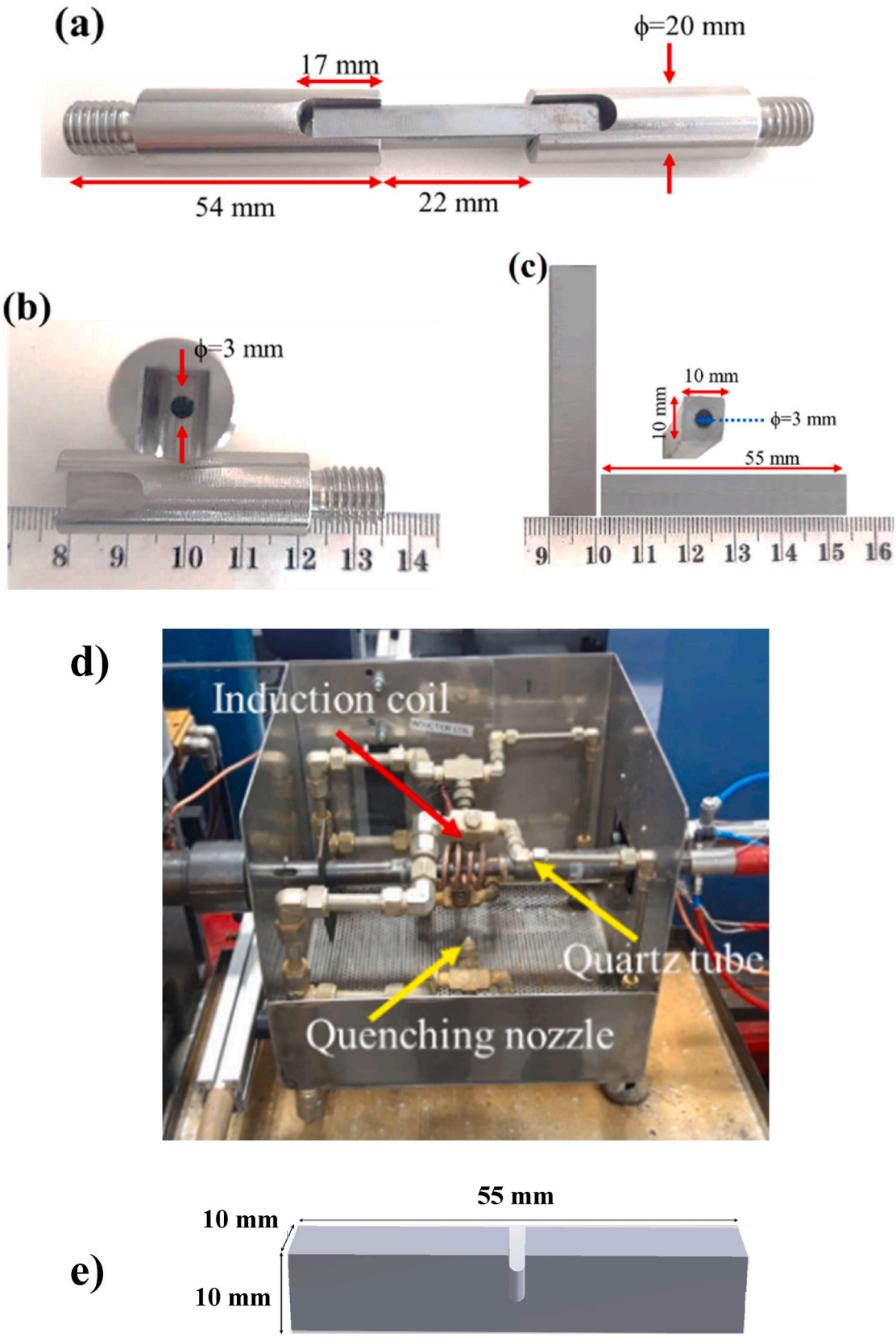

Fig. 1. (a) Experimental sample and sample holder consisted of three parts: (b) two-part sample holder and (c) rectangular sample. d) heat treatment set-up, showing induction furnace coil along with quartz tube, quenching nozzles and sample. f) schematic representation of impact testing specimen, having a U-notch grove made by wire-cut machine on the heat-treated rectangular sample.

Wombat, at the Australian Nuclear Science and Technology Organisation (ANSTO) [28]. For high temperature measurements, temperature control was achieved using a high temperature vacuum furnace with Nb heating elements. A cylindrical specimen of diameter 6 mm and length 70 mm was screwed into the base of a high temperature vacuum furnace centre stick and a thermocouple mounted in the hot zone just above the specimen. The sample was initially heated at 600 °C/h to 200 °C, and then at 180 °C/h to 1100 °C, followed by an isothermal hold at 1100 °C for 30 min. Afterwards, the sample was cooled at a rate of 180 °C/h to 300 °C, and then the furnace was turned off while the sample cooled to room temperature. A full beam height of 5 cm was used, and data were collected every minute throughout the process. Here, data in the cooling schedule from 1100 °C to 790 °C (just above austenite to ferrite transformation temperature) were only used to determine the lattice parameter of austenite upon cooling.

Two martensitic samples produced from coarse and fine parent austenite grains were used to measure the lattice parameter of martensite at different temperatures. It is well known that increased temperature leads to dislocation annihilation and carbide precipitation (*i.e.*, tempering) in the martensitic microstructure, affecting the lattice parameter. To probe these effects in isolation, the lattice parameter of martensite was measured upon cooling below room temperature. Each sample was cylindrical with a 6 mm diameter and 22 mm length, and inserted into a vanadium flanged can of diameter slightly greater than 6 mm that was closed but not sealed, and heating/cooling achieved in a top loading cryofurnace. The sample was attached to a cryofurnace centrestick equipped with a copper block at the top and bottom of the sample into which cartridge heaters were countersunk, with a thick conducting copper arm between them. A silicon diode temperature sensor was affixed to the top and bottom of the copper block and a radiative heat shield surrounded the sample. The sample well was filled with 10 mbar of He and temperature control achieved mainly using the cryostat wall temperature. In this experiment, the beam height was set at the sample height and data were collected every minute, starting with the whole system at ambient temperature and then switching the compressor to the cryostat on (a closed cycle He system) with a target temperature of −223 °C. Setpoints for the sensors at the top and bottom of the sample were set to −173 °C. All neutron data were collected at a neutron wavelength of 1.54060(2) Å, determined using the National Institute of Standards and Technology's (NIST) $La^{11}B_6$ standard reference material 660b. Data were analyzed using Pawley refinement with the TOPAS software [29] (see appendix A).

3. Results

The temperature at which the phase transformation started and finished was determined using dilatometry upon heating/cooling. The dilatometric curve of steel during continuous heating and cooling was plotted as a function of the temperature at the heating rate of 1 °C/s (Fig. 2a). The shape of the dilatometric curve indicates an alteration to the ambient structure as a result of the thermal treatment. The temperature for the austenite phase start/finish Ac_1 and Ac_3, respectively, was determined by the abrupt change in slope in the curve during heating, the temperature for the martensite phase start/finish M_s and M_f, respectively, was determined from the cooling data, as shown in Fig. 2a. During heating from room temperature, a linear behavior was observed up to ~700 °C above which the slope abruptly became negative until ~900 °C (Fig. 2a), followed by a sudden change to a positive slope. The linear behaviour corresponds to the thermal expansion of the steel, with the first slope change arising at Ac_1 from the initiation of the austenite transformation leading to significant volume contraction. With further temperature increase, the fraction of austenite progressively increases, resulting in a further decrease in volume until the complete transformation to austenite at Ac_3. After the completion of the transformation to austenite, the curve again becomes linear as a result of the thermal expansion of austenite. Upon cooling, the slope of the curve abruptly

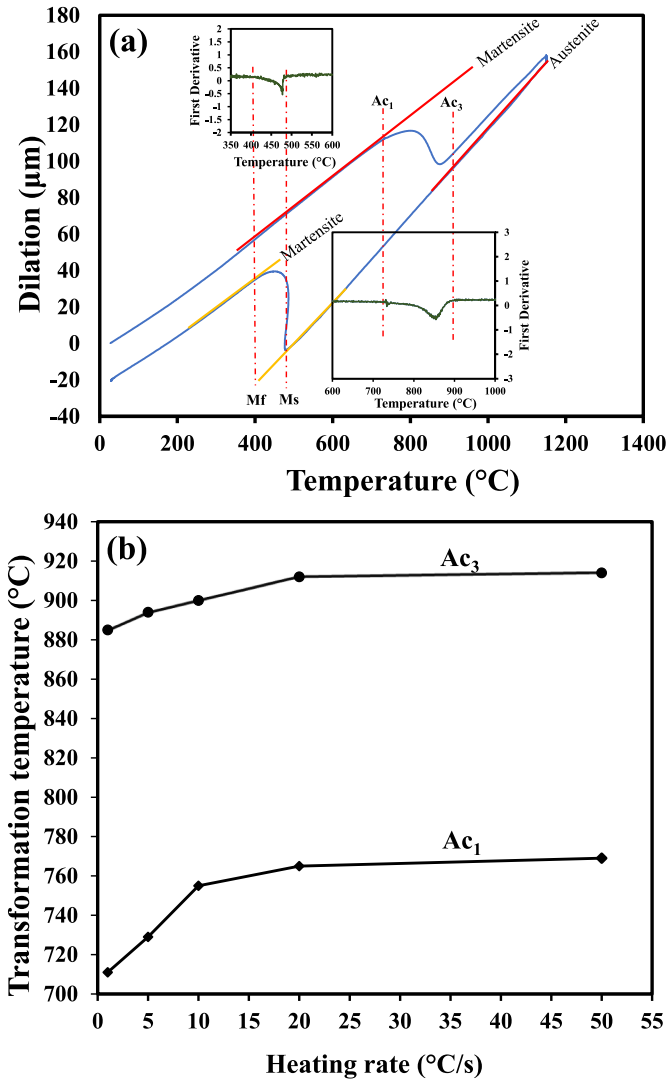

Fig. 2. (a) Dilation as a function of temperature during heating and cooling cycle (blue line). The critical start and finish austenite and martensite transformation temperatures were highlighted in the dilation curve achieved by 1 °C/s heating rate, where the linear behaviour of dilation curve abruptly changes (the intersection of solid and dash red lines). (b) Effect of heating rate on the Ac_1 and Ac_3 transformation temperatures (lines through points are a guide to the eye). The dilatometry test was performed once for each heating rate condition. (For interpretation of the references to colour in this figure legend, the reader is referred to the Web version of this article.)

altered twice in the range 400–500 °C, corresponding to the martensite transformation. To determine the critical phase transformation temperatures during heating/cooling, the first derivation of the dilation curve (dV/dT) was used, where deviations from linearity indicate start and finish temperatures for a given phase transformation (i.e., Ac_1, Ac_3, M_s, and M_f, in Fig. 2a). Ac_1, Ac_3, M_s, and M_f were found at 711, 885, 481, and 430 °C, respectively, for heating at 1 °C/s followed by cooling under Ar. The critical transformation temperature was measured for different heating rates (i.e., 1, 5, 10, 20, and 50 °C/s) (Fig. 2b). The heating rate influenced the start and finish austenite transformation temperature, which increased with heating rate, for example, Ac_3 was 885 °C at 1 °C/s and increased to 912 °C at 20 °C/s.

Grain refinement through cyclic heat treatment: Cyclic heat treatment led to the refinement of parent austenite grains (Figs. 3 and 4a). The parent austenite grain size was measured to be 84.0 ± 0.5 µm in the first cycle. The extent of parent austenite grain refinement was significant, reducing by the third cycle to 5.2 ± 0.2 µm, with subsequent thermal

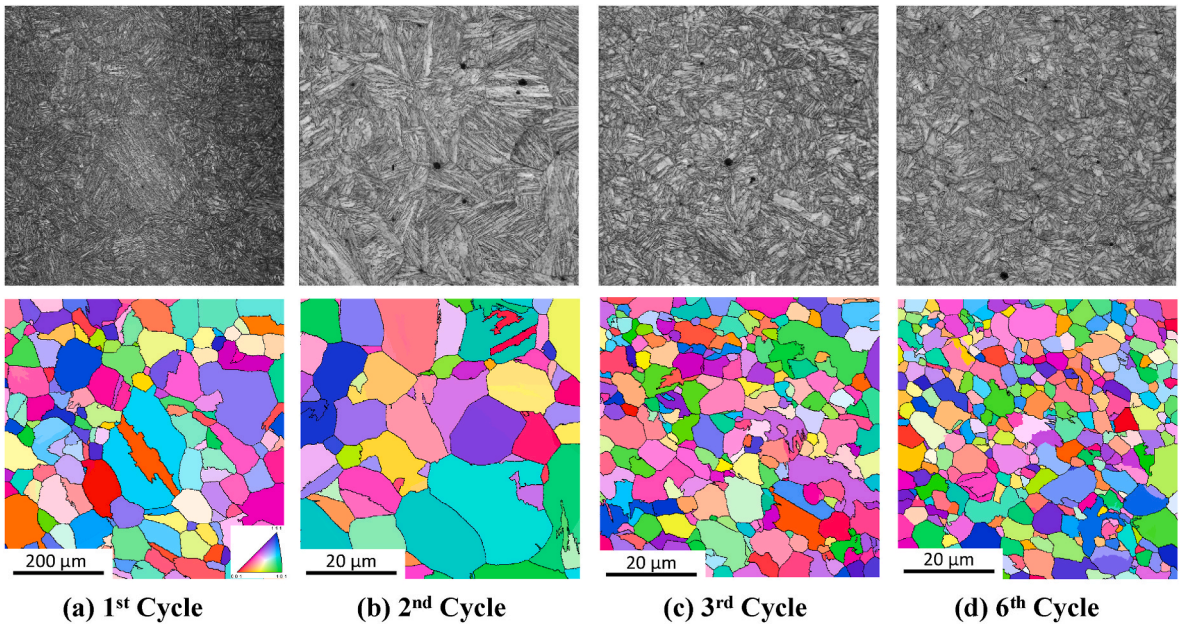

Fig. 3. The band contract image for martensitic microstructures transformed from austenite subjected to different cyclic heat treatments above Ac_3 temperature and their corresponding reconstructed parent austenite grain structures using TSL OIM V8 software. Austenite grain boundaries are identified by black lines. The reconstructed grain shapes sometime deviate from the simple polygonal shapes that are expected. While this suggests some inaccuracy in the reconstruction procedure, the average grain size is not expected to be greatly influenced by small errors in the grain boundary positions. The triangle inset in (a) represents colour codes referring to the normal direction. (For interpretation of the references to colour in this figure legend, the reader is referred to the Web version of this article.)

cycles having a lower rate of grain size refinement. The minimum parent austenite grain size was achieved after 6 thermal cycles (3.0 ± 0.1 µm), beyond which no change in the grain size was observed (Fig. 4a).

Critical martensitic transformation temperature: The experimental results show that start (M_s) and finish (M_f) martensitic transformation temperature reduced through refinement of the austenite parent phase (Fig. 4c). A significant change in M_s and M_f was observed between cycle 1 and 6, with further cycling having an almost insignificant effect, consistent with the reduction in austenite grain size.

Intervariant boundary population: Given the ~0.04 wt% carbon content in the steel, the Kurdjumov–Sachs (K–S) orientation relationship (OR) was assumed to govern the austenite to martensite phase transformation [17,22,23]; there are 24 K–S variants that can be theoretically formed within a single austenite grain (Table 1). These variants can be classified into four groups with a common close-packed plane, consisting of six individual variants V_1 to V_6 having different directions. The intersection of these variants hypothetically leads to 23 lattice misorientations, which can be reduced to 16 distinct intervariant boundaries due to crystal symmetry. Therefore, each individual parent austenite grain can be partitioned by specific boundaries, as listed in Table 1, which can be used to determine microstructure constituents as packets and blocks. The interaction of two distinct variants with the same habit plane leads to the formation of block boundaries (i.e., V_1–V_2 to V_1–V_6 in Table 1), whereas packet boundaries are formed by the impingement of two distinct variants from different families. Therefore, the blocks were delineated using all boundaries with a misorientation angle greater than 5° (i.e., all intervariant boundaries listed in Table 1 and prior austenite grain boundaries). To determine the packets, the lattice misorientations associated with the block boundaries were excluded from the boundary network. The block and packet sizes were then measured using the linear intercept method. According to this classification, the average block and packet size progressively decreased by the refinement of parent austenite grain size. The average diameter of each block and packet of coarse parent austenite grains (~84 µm diameter) is 5 ± 0.18 µm and 18 ± 0.40 µm, respectively. However, the average block and packet size reduced to 2 ± 0.04 µm and 3 ± 0.05 µm, respectively, for the fine parent austenite grains (~3 µm diameter, Fig. 4b). In turn, the overall hardness increased from 314 ± 0.6 $HV_{10\ kgf}$ to 343 ± 0.5 $HV_{10\ kgf}$ for the martensite transformed from coarse and fine parent grain size, respectively.

The distribution of misorientation angles in the transformed lath martensite microstructure of the coarse parent austenite grain (84 ± 0.5 µm diameter) features two maxima in the 5–22° and 46–60° range, in good agreement with the theoretical misorientation angles expected from the K–S OR theory (Fig. 5a and Table 1). The distribution of misorientation angles in the range 23–45° stems from parent austenite grain boundaries, where variants on either side of boundaries do not follow the K–S OR (Fig. 5 and Table 1). The parent austenite grain size significantly changed the misorientation angle distribution in the lath martensitic microstructure. The most striking change related to boundaries is in the range 46–60°, where the population progressively decreased with parent austenite grain size refinement. For example, the population of boundaries with a misorientation angle of 60° was 20 % in the sample with a 84 µm grain size (Fig. 5a), but only 6 % in the sample with a 3 µm grain size (Fig. 5d). By contrast, parent austenite grain size refinement enhanced the population of boundaries with misorientation in the range 23–45° (i.e., non-KS boundaries).

The intervariant boundary plane distribution revealed that intervariant boundaries following K–S OR theory largely terminated at {110} planes, and were twist, tilt, or mixed type (Appendix B and Table 1). Although significantly altering the population, the parent austenite grain size appeared to have no pronounced effect on the character of intervariant boundaries. In general, the intervariant boundary with a 60°/[011] misorientation was most common with the highest intervariant length fraction in the grain followed by the 60°/$[11\bar{1}]$, 10.5°/$[0\bar{1}\bar{1}]$, and 57.2°/$[\bar{3}56]$ misorientations (Fig. 6a). The first three intervariant boundaries with the highest fraction share the same habit plane (V_1–V_3, V_1–V_2, and V_1–V_4, Table 1). Refinement of the parent austenite grain size led to a significant change in distribution of the intervariant boundaries, the most noticeable being for the 60°/[011] intervariant boundary whose population reduced from ~76.9 % in coarse grains (i.e., ~84 µm diameter) to ~ 37.9 % for smaller grains (~3 µm diameter). The 57.2°/$[\bar{3}56]$ intervariant boundary had a relatively

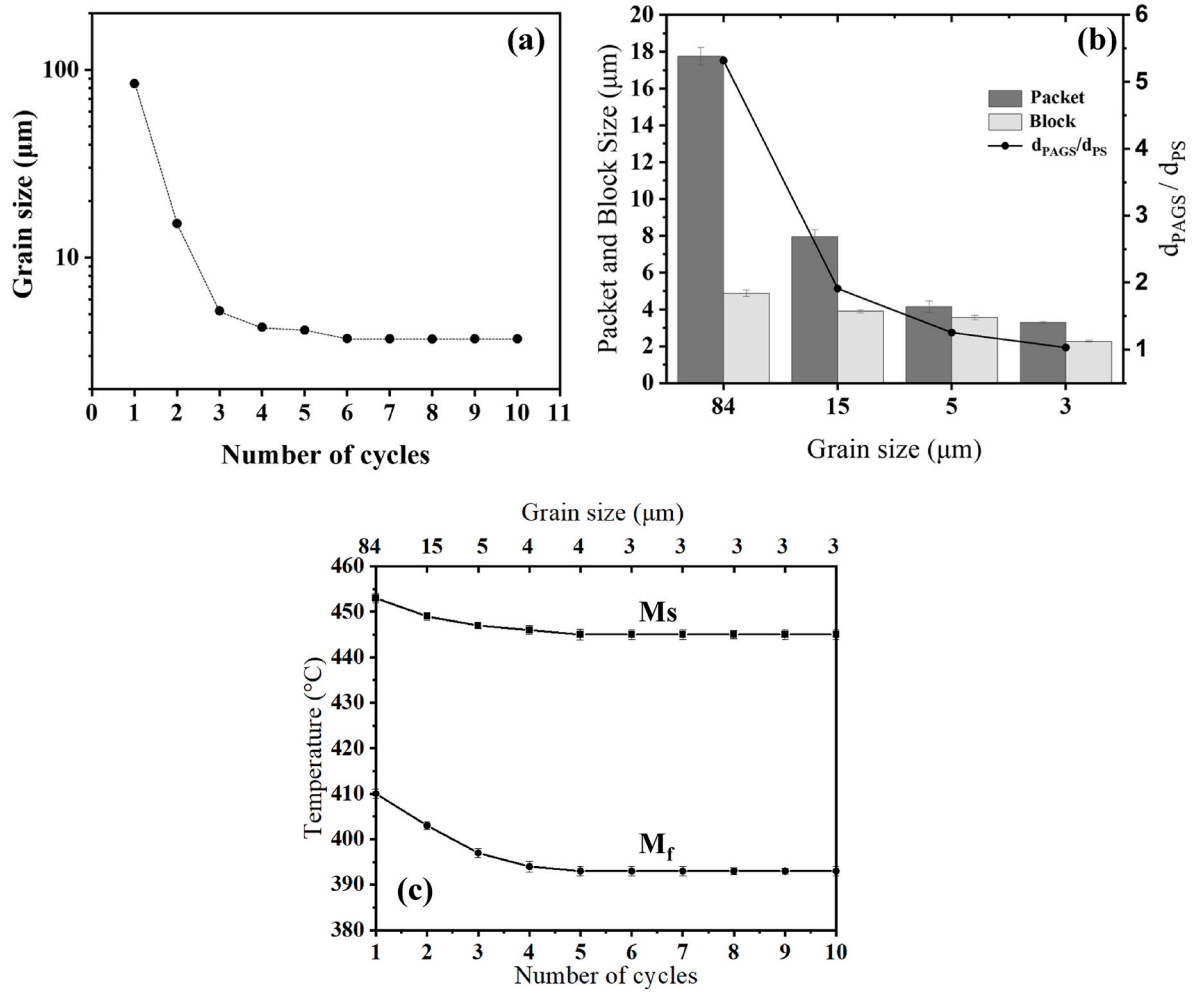

Fig. 4. The effect of number of thermal cycles on (a) the parent austenite grain size (d_{PAGS}), (b) packet size (d_{PS}), block size and the ratio of the parent austenite grain size over packet size for the microstructure produced from different parent austenite grain sizes during thermal cycling. (c) The effect of thermal cycling (parent austenite grain size) on the martensite start and finish temperature. Errors are smaller than the points and lines through the points are a guide to the eye.

smaller population reduction, with other intervariant boundaries (e.g., 10.5°/[11$\bar{1}$], 14.8°/[13 5 1], 50.5°/[$\bar{1}$0 3 $\bar{1}$3], and 51.7°/[$\bar{1}$1 6 $\bar{1}$1]) slightly increasing in fraction with parent austenite grain refinement.

The total length of K–S OR intervariant boundaries and [110] twist boundaries, where the grain boundary plane normal is parallel to the misorientation axis (i.e., consisted of 10.5°/[0$\bar{1}$1], 49.5°/ [011] and 6 0°/ [011] intervariant boundaries), decreased by refining the parent austenite grain size. However, the grain refinement led to a progressive increase in the total length of the [111] tilt boundaries where the grain boundary plane normal is perpendicular to the misorientation axis (i.e., consisted of 10.5°/[11$\bar{1}$], 49.5°/[$\bar{1}$1$\bar{1}$] and 6 0°/[11$\bar{1}$] intervariant boundaries Fig. 6b). The length per unit area of all 16 K–S OR intervariant boundaries decreased from 1.12 μm/μm^2 to 0.67 μm/μm^2 with reduced parent austenite grain size from diameter ~84 μm–~3 μm, respectively. Intervariant boundaries with a [110] misorientation axis also reduced with parent austenite grain size, decreasing their length per unit area from 0.90 to 0.33 μm/μm^2 for grains with diameter ~ 84 μm and ~3 μm, respectively. However, reduction in the austenite grain diameter from ~84 μm to ~3 μm led to an increase in the length per unit area of intervariant boundaries with a [111] misorientation axis, increasing from 0.06 to 0.16 μm/μm^2, respectively (Fig. 6b).

Connectivity of the intervariant boundary network: The boundary network connectivity was investigated using a homology metrics approach. Here, the topology parameters (Betti numbers) β_0 and β_1 were measured. β_1 defines the continuous and closed paths of the boundaries and β_0 refers to separate boundary segments in the rest of the network. The inverse connectivity of the boundary network can be characterised by β_0/β_1, known as β_{01}, within a given microstructure [14,16,30]. In this way, the connectivity of the intervariant boundaries was established for misorientation angles, excluding those ranging from 23 to 45° which contain non-KS boundaries (Table 1). The grain boundary network connectivity was affected by the refinement of the parent austenite grain size. In general, the inverse boundary network connectivity was enhanced by an increased misorientation angle threshold for all conditions, however, parent austenite grain refinement led to a decrease in the connectivity of K–S OR intervariant boundaries (Fig. 7a). A similar trend was observed for [110] twist boundaries, revealing reduced connectivity with parent austenite grain refinement (Fig. 7b). The intervariant boundary network connectivity of [111] boundaries with a symmetrical tilt character increased with parent austenite grain refinement (Fig. 7c).

In situ neutron diffraction: In situ neutron powder diffraction data of austenite at 1100 °C and 790 °C could be fully indexed to austenite (γ-phase Fe) (Fig. 8a). The lattice parameter of the sample linearly varied between 3.66903(58) Å at 1100 °C to 3.64339(57) Å at 790 °C (Fig. 8b). The high temperature evolution of the lattice parameter was extrapolated to M_s for different parent austenite grain sizes, yielding estimates of 3.6134(4) Å at 445 °C (for fine grains) and 3.61404(47) Å at 453 °C (for coarse grains).

In situ neutron powder diffraction data of fine and coarse parent

Table 1
The 24 possible variants generated through phase transformation having the KS orientation relationship [5].

Variant	Plane Parallel	Direction Parallel	Rotation angle/axis from V1	Character	Plane normal/s
V1	$(111)_\gamma \| (0\ 11)_\alpha$	$[\bar{1}01]_\gamma \| [\bar{1}\bar{1}1]_\alpha$	–	–	–
V2		$[\bar{1}01]_\gamma \| [\bar{1}1\bar{1}]_\alpha$	60°/[11$\bar{1}$]	Symmetry Tilt[a]	($\bar{1}$1 0), (011), (1 01), (1$\bar{1}$ 0)
V3		$[0\ 1\bar{1}]_\gamma \| [\bar{1}\bar{1}1]_\alpha$	60°/[0 11]	Twist[b]	(0 11)
V4		$[0\ 1\bar{1}]_\gamma \| [\bar{1}1\bar{1}]_\alpha$	10.53°/[0 $\bar{1}\bar{1}$]	Twist	(0 $\bar{1}$ $\bar{1}$)
V5		$[1\bar{1}\ 0]_\gamma \| [\bar{1}\bar{1}1]_\alpha$	60°/[0 $\bar{1}\bar{1}$]	Twist	(0 $\bar{1}$ $\bar{1}$)
V6		$[1\bar{1}\ 0]_\gamma \| [\bar{1}1\bar{1}]_\alpha$	49.47°/[0 11]	Twist	(0 11)
V7	$(1\bar{1}1)_\gamma \| (0\ 11)_\alpha$	$[1\ 0\bar{1}]_\gamma \| [\bar{1}\bar{1}1]_\alpha$	49.47°/[$\bar{1}\bar{1}$1]	Symmetry Tilt	($\bar{1}$1 0), (011), (1 01), (1$\bar{1}$ 0)
V8		$[1\ 0\bar{1}]_\gamma \| [\bar{1}1\bar{1}]_\alpha$	10.53°/[11$\bar{1}$]	Symmetry Tilt	($\bar{1}$1 0), (011), (1 01), (1$\bar{1}$ 0)
V9		$[\bar{1}\bar{1}0]_\gamma \| [\bar{1}\bar{1}1]_\alpha$	50.51°/[$\bar{1}$0 3 $\bar{1}$3]	Mixed[c]	(1 01)
V10		$[\bar{1}\bar{1}0]_\gamma \| [\bar{1}1\bar{1}]_\alpha$	50.51°/[$\bar{7}$ $\bar{5}$ 5]	Mixed	(1 01)
V11		$[0\ 11]_\gamma \| [\bar{1}\bar{1}1]_\alpha$	14.88°/[13 5 1]	Mixed	(0 11)
V12		$[0\ 11]_\gamma \| [\bar{1}1\bar{1}]_\alpha$	57.21°/[$\bar{3}$ 5 6]	Mixed	(1 01)
V13	$(\bar{1}11)_\gamma \| (0\ 11)_\alpha$	$[0\bar{1}1]_\gamma \| [\bar{1}\bar{1}1]_\alpha$	14.88°/[5 $\bar{1}\bar{3}$ $\bar{1}$]	Mixed	(0 11)
V14		$[0\bar{1}1]_\gamma \| [\bar{1}1\bar{1}]_\alpha$	50.51°/[$\bar{5}$ 5 $\bar{7}$]	Mixed	(1 01)
V15		$[\bar{1}0\bar{1}]_\gamma \| [\bar{1}\bar{1}1]_\alpha$	57.21°/[$\bar{6}$ $\bar{2}$ 5]	Mixed	($\bar{1}$ 01)
V16		$[\bar{1}0\bar{1}]_\gamma \| [\bar{1}1\bar{1}]_\alpha$	20.61°/[11 $\bar{1}\bar{1}$ $\bar{6}$]	Mixed	(0 11), ($\bar{1}$ 01)
V17		$[11\ 0]_\gamma \| [\bar{1}\bar{1}1]_\alpha$	51.73°/[$\bar{1}\bar{1}$ 6 $\bar{1}\bar{1}$]	Mixed	(0 11), ($\bar{1}$ 01)
V18		$[11\ 0]_\gamma \| [\bar{1}1\bar{1}]_\alpha$	47.11°/[$\bar{2}\bar{4}$ $\bar{1}\bar{0}$ 21]	Mixed	($\bar{1}$ 01)
V19	$(11\bar{1})_\gamma \| (0\ 11)_\alpha$	$[\bar{1}10]_\gamma \| [\bar{1}\bar{1}1]_\alpha$	50.51°/[$\bar{3}$ 13 10]	Mixed	(1 01)
V20		$[\bar{1}10]_\gamma \| [\bar{1}1\bar{1}]_\alpha$	57.21°/[3 6 $\bar{5}$]	Mixed	(1 01)
V21		$[0\ \bar{1}\bar{1}]_\gamma \| [\bar{1}\bar{1}1]_\alpha$	20.61°/[3 0 $\bar{1}$]	Mixed	(0 11), (0 $\bar{1}$1)
V22		$[0\ \bar{1}\bar{1}]_\gamma \| [\bar{1}1\bar{1}]_\alpha$	47.11°/[$\bar{1}$0 21 24]	Mixed	($\bar{1}$ 01)
V23		$[1\ 01]_\gamma \| [\bar{1}\bar{1}1]_\alpha$	47.21°/[$\bar{2}\bar{5}\bar{6}$]	Mixed	($\bar{1}$ 01)
V24		$[1\ 01]_\gamma \| [\bar{1}1\bar{1}]_\alpha$	21.06°/[9 $\bar{4}$ 0]	Mixed	(0 11), (0 $\bar{1}$1)

[a] **Symmetry Tilt**: the grain boundary plane normal is perpendicular to the rotation axis (i.e., [11$\bar{1}$]).
[b] **Twist:** the grain boundary plane normal is parallel to the rotation axis (i.e., [110]).
[c] **Mixed:** the grain boundary whose plane normal is neither parallel nor perpendicular to the rotation axis.

austenite grain samples at 0 and -90 °C could be fully indexed to martensite (Fig. 8c). The lattice parameter changed linearly with temperature for both samples, however, thermal contraction was modulated by the microstructure (Fig. 8d). The lattice parameter extrapolated to M_s for the fine and coarse parent austenite grains was 2.89210(2) Å at 445 °C (fine grains) and 2.89949(5) Å at 453 °C (coarse grains).

The linear coefficient of thermal expansion (CTE) of martensite is calculated $\frac{1}{a}\left(\frac{da}{dT}\right)$ where a and T represent lattice parameter and temperature, respectively. It appeared that the change in the parent austenite grain size modulated the linear coefficient of thermal expansion (CTE) of martensite from $3.00(2) \times 10^{-5}$ Å/°C to $2.00(8) \times 10^{-5}$ Å/°C for 84 μm and 3 μm parent austenite grain sizes, respectively (Fig. 8d). The CTE is a key parameter determining a material's dimensions and residual stresses during heating and cooling processes. Although the CTE is influenced by the composition and microstructure characteristics such as grain size in different materials [31,32], it is not clear how the parent grain size influences the CTE of the transformed products such as martensite, which are widely used in applications undergoing thermal cycling (i.e., pipelines and vessel). However, this is out of current study scope, and requires further investigation.

4. Discussion

Successive martensite-to-austenite transformations through multiple heat treatment cycles appear to significantly refine the parent austenite grain size, which in turn influences the subsequent martensitic transformation characteristics M_s and M_f and microstructure constituents, namely the martensite block and packet size, as well as the intervariant boundary network (i.e., population and connectivity). The steel microstructure completely transforms to single phase austenite on reheating above Ac_3, where austenite is expected to nucleate at high energy regions (e.g., grain boundaries), influencing austenite grain size via the number of austenite nucleation sites with more sites leading to a finer microstructure [24]. Therefore, a fine martensitic microstructure promotes nucleation sites, parent austenite grain boundaries, as well as block and packet boundaries, restricting the growth of austenite and yielding a smaller grain size and eventually finer martensite on quenching [24,33]. The latter promotes further austenite nucleation sites during subsequent cycling heat treatments, resulting in a progressive refinement of austenite grain size (Figs. 3 and 4a). However, there is an apparent ~3 μm limit to the diameter of austenite grain size due to competition between austenite nucleation and the growth rate [34] (Fig. 4a).

Parent austenite grain refinement reduces the critical martensitic phase transformation temperatures M_s and M_f, which decrease with decreasing grain size (Fig. 4c). This trend is different from ferrite, diffusional transformation, where the start (Ar_3) and end (Ar_1) transformation temperatures increase as the grain size is reduced due to the increased concentration of nucleation sites [35]. This could arise from differences in the martensitic phase transformation mechanism (shear/displacive) [24]. The shear transformation is accompanied by elastic strain, which can be accommodated through the formation of specific variant arrangements in the martensite. In coarse parent austenite grains, multiple variants can form and reduce elastic strain. Austenite grain refinement reduces the volume in which martensite variants can form, restricting the number of variants during the martensitic transformation. This may ultimately promote specific variant arrangements that accommodate the strain associated with the martensitic transformation, as discussed in detail later, leading to lower M_s and M_f [24,26] (Fig. 4c). A decrease in the transformation temperature due to austenite grain refinement enhances strength, restricting the growth of martensite variants, eventually leading to finer martensite constituents (i.e., packet and block size, Fig. 4b) [26]. This results a reduction in the parent austenite grain to packet size ratio, which approaches 1 at a parent austenite grain size of 3 μm (Fig. 4b).

The parent austenite grain size influences the martensite boundary network characteristics (i.e., population and connectivity, Figs. 6 and 7). The grain boundary network can be affected by several factors such as chemical composition [13,36,37], transformation mechanism [38], crystallographic texture [39,40], temperature and strain [7,18,41–43], and grain size [44]. Since the experimental samples have identical chemical composition and follow the same phase transformation, some

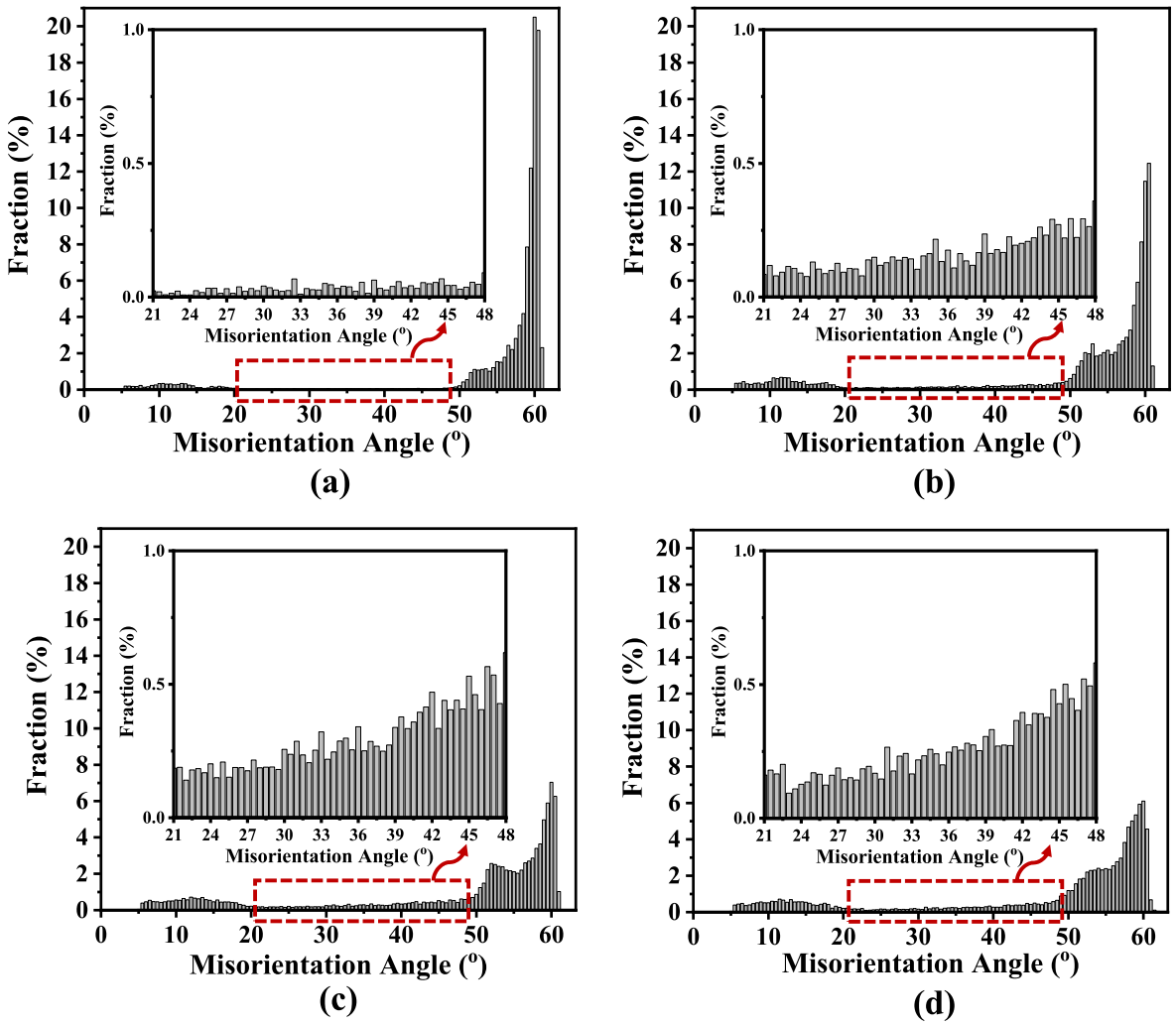

Fig. 5. Distribution of misorientation angles in the lath martensite microstructures with different parent austenite grain sizes; (a) ~ 84 μm, (b) ~ 15 μm, (c) ~ 5 μm, and (d) ~ 3 μm.

of these factors can be ruled out. We note qualitatively a similar crystallographic texture in samples before and after grain refinement (Fig. 9), due to texture memory effects [45,46]. Neutron powder diffraction data taken with an area detector revealed complete Debye Scherrer cones with no indication of crystallographic texture. However, changes in the intensity of orientation distribution function are noted with continued transformation cycling, reducing from ~3.4 MRD for martensite after the first cycle to ~1.3 MRD after six thermal cycles (Fig. 9).

Parent austenite grain refinement significantly alters the misorientation angle distribution, but the trend varies with misorientation angle (Fig. 5). The main factor responsible for this change is likely to be that the parent austenite grain boundary area increases with reduced grain size. This leads to an increased population of non-KS misorientations, ranging from 23° to 45°, since these boundaries are formed as a result of the intersection of variants belonging to two neighbouring grains with distinct orientation. Consequently, this decreases the population of boundaries with misorientations in the range 10°–22° and 46°–60° (Fig. 5), which are mostly the K–S misorientations.

The parent austenite grain size also changes the relative population of martensite intervariant boundaries. For instance, the populations of 60°/[11$\bar{1}$], 10.5°/[0$\bar{1}$1], 10.5°/[11$\bar{1}$], 50.51°/[$\bar{1}$0 3 $\bar{1}$3], and 14.88°/[13 5 1] boundaries increase with reduced parent austenite grain size, however the populations of 60°/[011], 49.47°/[110], and 57.21°/ [$\bar{3}$ 5 6] misorientations decrease (Fig. 6a). This suggests that the arrangement of variants changes during the martensitic transformation due to the grain refinement, which is expected as the parent grain size alters M_s and M_f (Fig. 4c). This results in a change in the lattice parameter of both the parent austenite and resultant martensite, as demonstrated by the lattice parameter measurement using *in situ* neutron powder diffraction (Fig. 8). The austenite and martensite lattice parameters extrapolated to M_s decreased from 3.61404(47) Å to 3.6134(4) Å and 2.89949(5) Å to 2.89210(2) Å for coarse and fine parent austenite grains, respectively, due to a decrease in M_s temperature from 453 °C (coarse grains) to 445 °C (fine grains). This influences elastic strain associated with the shear/displacive transformation [26,47], potentially influencing variant arrangement. To evaluate this, we employ the phenomenological theory of martensite crystallography (PTMC) that considers the lattice parameter of both parent austenite and martensite for fine and coarse parent austenite grains at M_s [48], deriving the lattice parameter from *in situ* neutron powder diffraction.

According to the PTMC with double invariant lattice shear mechanisms [13,49,50], the shape deformation matrix, Bain strain matrix, habit plane, shear direction, and shear magnitude, were calculated (Table 2), as described in Appendix C. The Von-Mises equivalent strain, ϵ_{VM}, is then determined by defining the overall transformation strain tensors (Eq. (1)) to identify the degree of self-accommodation for different variant cluster combinations (i.e., 2, 3, 4, 5 and 6 variant cluster arrangements).

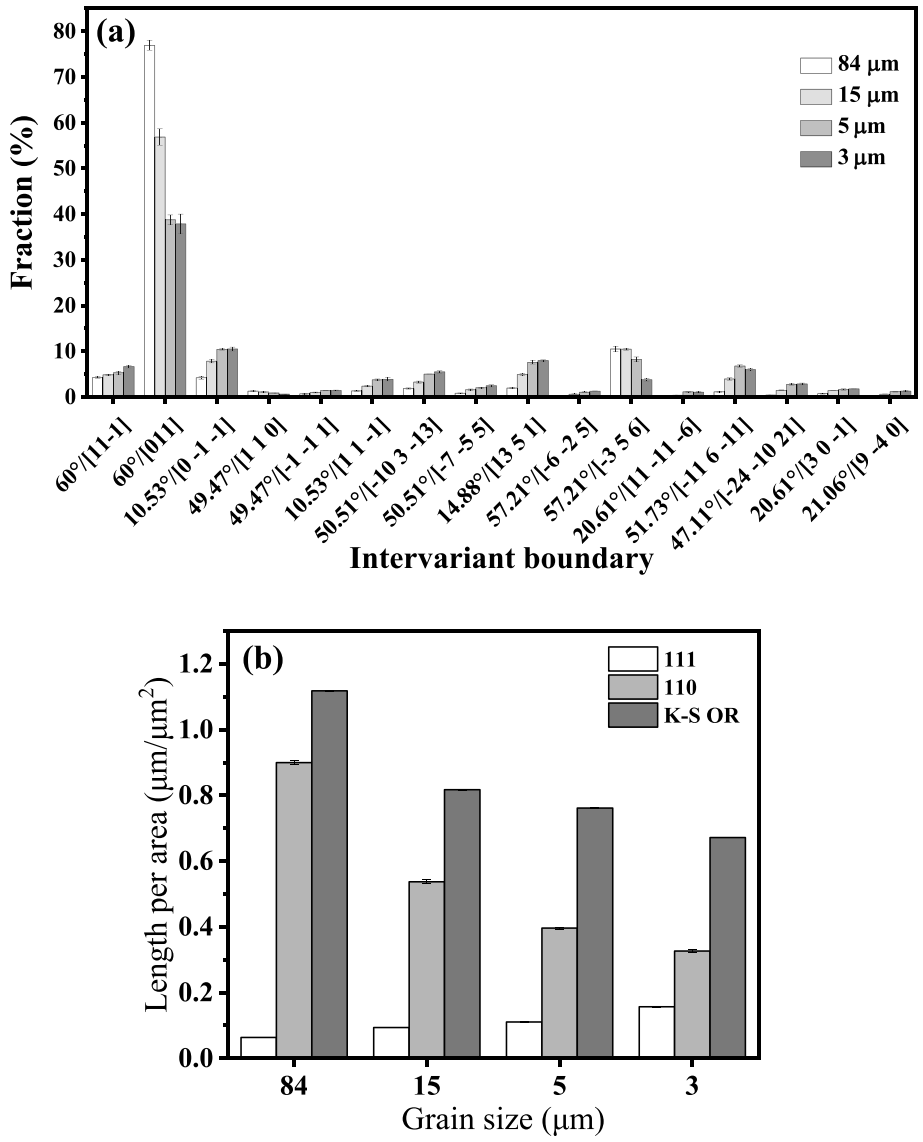

Fig. 6. (a) the fraction of intervariant boundaries in the lath martensite measured by TSL software considering 5° tolerance angle, and (b) the length per unit area (μm/μm^2) for intervariant boundaries associated with K–S OR listed in Table 1, [111] tilt character and [110] twist character for different parent austenite grain sizes.

$$\epsilon_{VM} = \sqrt{\frac{3}{2}\left[\left(T_{11}^2 + T_{22}^2 + T_{33}^2\right) + \frac{1}{2}\left(4T_{12}^2 + 4T_{13}^2 + 4T_{23}^2\right)\right]} \quad \text{Eq. 1}$$

where T_{11}, T_{22}, T_{33}, T_{12}, T_{13}, and T_{23} are strain tensors, *Tij* (Appendix C).

In the current study, there are 30, 120, 360, 720, and 720 different possible combinations for 2, 3, 4, 5, and 6 variant cluster arrangements, respectively, within a martensite packet. The combination of the Von-Mises equivalent strain from different variant clustering configurations is computed to estimate the average Von-Mises equivalent strain in both martensitic microstructures. The combination of different variants representing the minimum average strain (ϵ_{ave}) is shown in Table 3. The lattice parameter of martensite is significantly influenced by transformation temperature, which is lower for parent austenite with a smaller grain size. This ultimately affects the magnitude of inhomogeneous shear during martensite transformation (Table 2). Based on the phenomenological theory of martensite, the refinement of parent austenite grain size alters the martensite variant clustering from 3 variants ($V_1V_3V_5$ and $V_2V_4V_6$) for coarse grains to 4 variants (V_1V_2 V_3V_4) for fine grains. The former promotes the formation of 60°/ [110] boundaries, though the latter leads to the development of 60°/ [11$\bar{1}$], 10.5°/ [0$\bar{1}\bar{1}$], in addition to 60°/[110] intervariant boundaries (Table 1). The PTMC predicts that the austenite grain refinement promotes the population of 60°/[11$\bar{1}$], 10.5°/[0$\bar{1}\bar{1}$] boundaries at the expense of the 60°/[110] boundary, which is consistent with the experimental result (Fig. 6a). The minimum strain changed from 0.0506 in the coarse parent grain to 0.0478 in the fine parent grain (Table 3). We note that the combination of 5 and 6 variant clustering increase strain for both coarse and fine parent grains (Table 3), suggesting that these variant clustering arrangements need more energy to form.

Variant arrangements can be found in the coarse and fine grain microstructures that agree with the results of the PTMC calculation (Fig. 10). For example, the 3 variant clustering is frequently observed in the coarse martensitic microstructure (e.g., $V_8V_{10}V_{12}$ and $V_2V_4V_6$ in Fig. 10ac). An example of 4 variant clustering in a fine parent austenite grain (e.g., $V_{13}V_{14}V_{15}V_{16}$) is illustrated in Fig. 10d and e. However, these examples are not meant to imply that these are the only clusters observed; other variant arrangements, which do not necessarily have the lowest strain based on the PTMC (Table 3), are also observed in the microstructures. This discrepancy could be partly due to the incomplete nature of two-dimensional observations that do not fully represent three-dimensional arrangement of variants. In addition, the strain

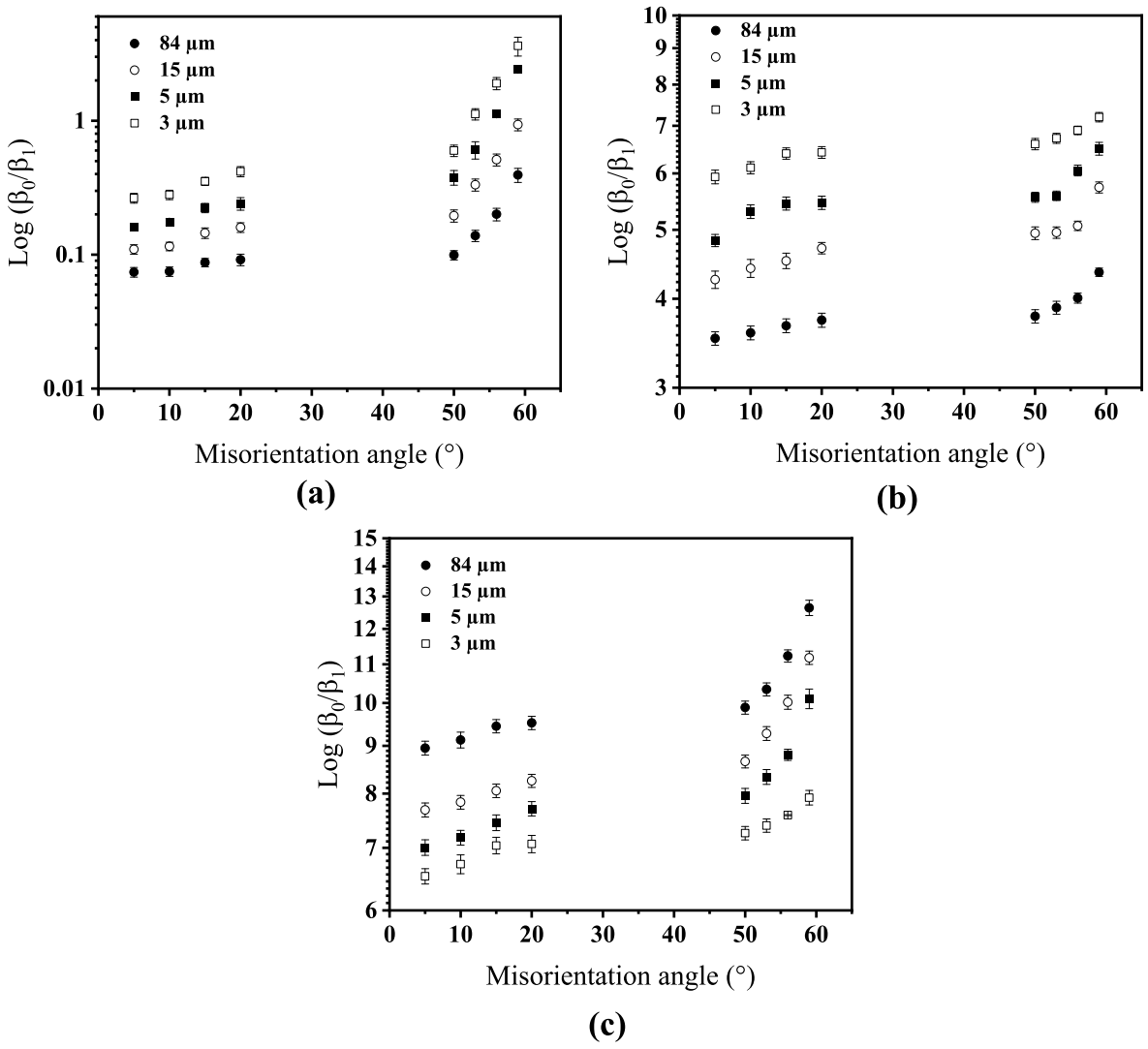

Fig. 7. Inverse connectivity of the boundary network as a function of misorientation angle threshold for different {110} boundaries for (a) all boundaries excluding the boundaries in the range of 23–45°, (b) twist boundaries, and (c) tilt boundaries.

difference between 4 variant and other variant arrangements, except 2 variant, is less than 7 % (Table 3), which makes it possible to form other variant configurations in some grains, as also observed locally in some coarse grain austenite structures (Fig. 10a).

Both the PTMC calculation and the observation of low strain variant groups are consistent with the observation that the refinement of parent austenite grain size leads to an increase in the population of 60°/ $[11\bar{1}]$ and 10.5°/$[0\bar{1}\bar{1}]$ intervariant boundaries at the expense of intervariant boundaries with 60°/[110] misorientation. The change in the variant selection mechanism due to parent austenite grain refinement also alters the connectivity of intervariant boundaries. In general, [110] twist boundaries have a connectivity that reduces with parent austenite grain refinement (Fig. 7b), due to a reduction in the population of 60°/ [110] boundary. By contrast, [111] symmetrical tilt boundaries had a connectivity that increased with parent austenite grain refinement as a result of increasing population of 60°/[111] boundaries (Fig. 7c). In both cases, the greater the concentration of a certain boundary type, the more likely they are to intersect and form a more connected network.

To understand the role of grain boundary network on material performance, the impact toughnesses of the martensitic microstructures produced from distinct parent austenite grain size was evaluated. It appears that the change in the parent austenite grain size also alters the room temperature impact toughness, increasing from 75 ± 1 J to 86 ± 2 J with a decrease in the parent austenite grain size from 84 µm to 3 µm, respectively. Although the difference is relatively low at ambient temperature and their fracture surfaces, dominated by abundant dimples, indicate ductile failure, the coarse grained microstructure occasionally exhibited the presence of a few cleavage facets (Fig. 11). One of the criteria to determine the propensity of a boundary to promote the initiation and propagation of a crack is the grain boundary energy (i.e., high energy boundaries are detrimental to the toughness and vice versa) [51]. We calculated the energy of intervariant boundaries formed through martensitic transformation using molecular statics simulations [5]. In short, a boundary structure database was generated for different intervariant boundaries by in-house Python code. It was assumed that the martensite has a body-centred cubic structure due to the low carbon content [16]. In addition, the presence of alloying elements (e.g., C) was not considered and the simulation was performed using pure iron. The energy of boundaries was minimised and measured by a large-scale atomic/molecular massively parallel simulator (LAMMPS) [52] using Fe–H potential in Ref. [53]. The simulation revealed that the intervariant boundaries display a wide range of energies from 306 to 1109 mJ/m^2, where the 60°/[111] symmetric tilt exhibits the lowest energy and mixed boundaries largely show the highest energy [5]. The former is a relatively small fraction, which progressively increases with the refinement in the parent austenite grain size (Fig. 6a). Mixed boundaries

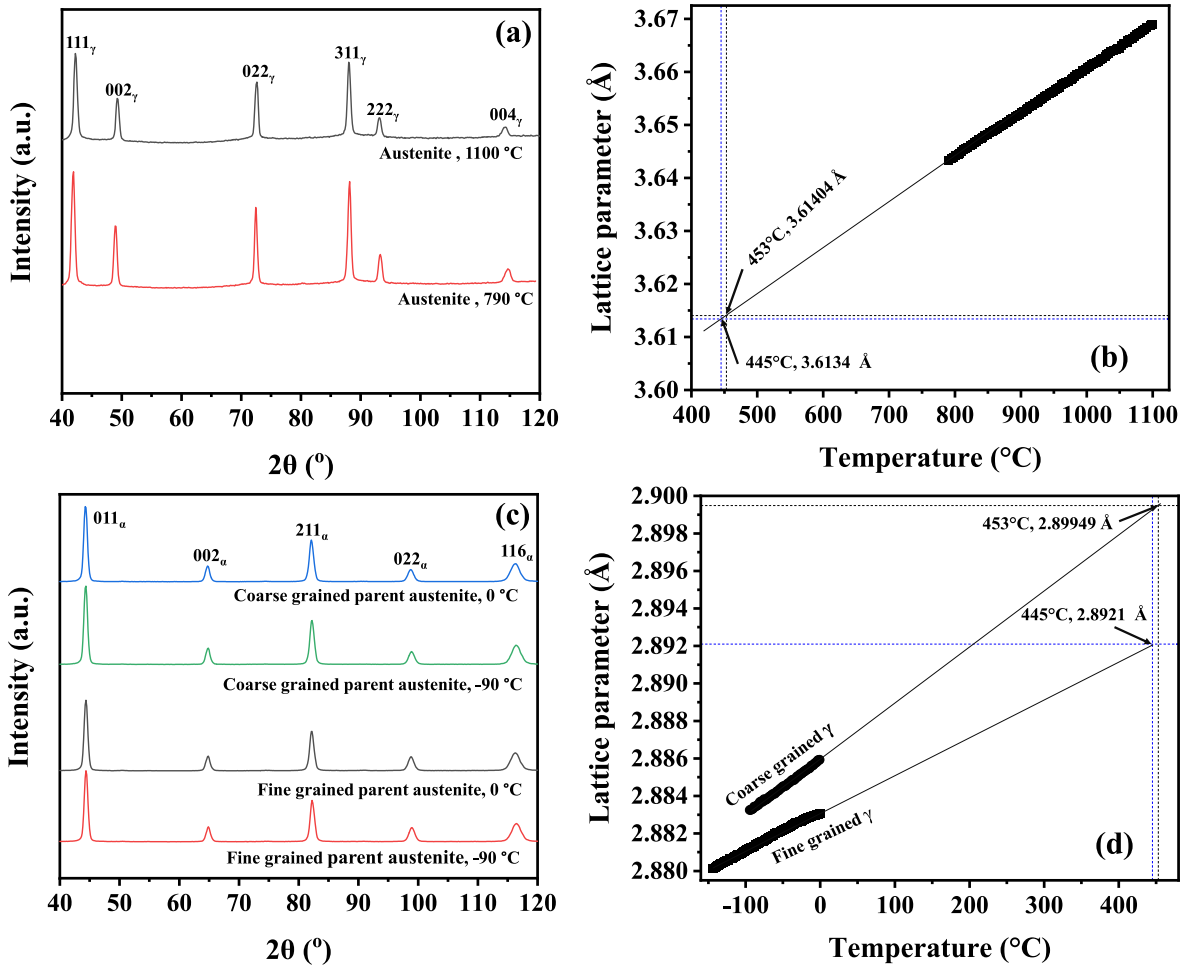

Fig. 8. (a) *In situ* neutron powder diffraction data for austenite at 1100 °C and 790 °C, offset in y for clarity. (b) temperature dependence of the austenite lattice parameter, extrapolated to *Ms* for fine (445 °C) and coarse (453 °C) parent austenite grain microstructures (intersection of solid black line and dashed blue lines). (c) In situ neutron powder diffraction data for martensite at 0 °C and −90 °C, from fine and coarse parent austenite grains, offset in y for clarity. (d) temperature dependence of the martensite lattice parameter for fine and coarse parent austenite microstructures, extrapolated to *Ms* for fine (445 °C) and coarse (453 °C) parent austenite grain microstructures (intersection of solid black line and dashed blue lines). a.u. is arbitrary units. (For interpretation of the references to colour in this figure legend, the reader is referred to the Web version of this article.)

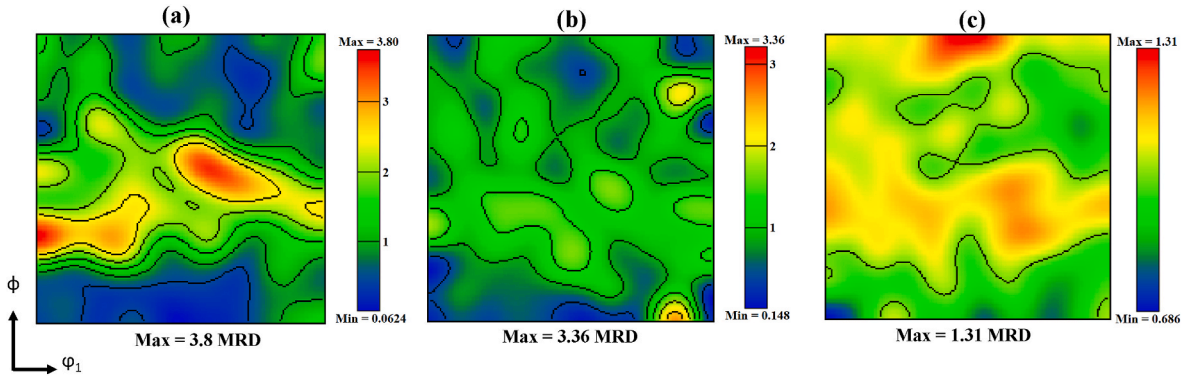

Fig. 9. The orientation distribution function (ODF) at $\varphi 2 = 45^{\circ}$ for (a) initial hot rolled, and martensite transformed from (b) coarse (~84 μm), and (c) fine (~3 μm) parent austenite grain microstructures. MRD represents multiples of a random distribution.

Table 2
The typical calculated crystallographic sets based on the PTMC calculations.

	Coarse microstructure	Fine microstructure
Lattice parameters	$a_{\alpha} = 2.89949$ Å $a_{\gamma} = 3.61404$ Å	$a_{\alpha} = 2.8921$ Å $a_{\gamma} = 3.6134$ Å
Shear system	S1: $<\bar{1}10>_{\gamma}(\bar{1}11)_{\gamma}$ S2: $<\bar{1}10>_{\gamma}(1\bar{1}2)_{\gamma}$	
Bain strain	[1.13464 0.0000 0.0000 0.0000 1.1346 0.0000 0.0000 0.0000 0.8023]	[1.1319 0.0000 0.0000 0.0000 1.1319 0.0000 0.0000 0.0000 0.8004]
Shear direction	$<\overline{0.4182}\ \overline{0.6008}\ \overline{0.6813}>_{\gamma}$	$<\overline{0.5412}\ 0.4671\ 0.9662>_{\gamma}$
Shear magnitude	0.2248 $S_1 = 0.0006$ $S_2 = 0.2775$	0.2470 $S_1 = 0.0251$ $S_2 = 0.2446$
Shear deformation	[1.0604 0.0742 0.1050 0.0748 1.0604 −0.1052 −0.0742 0.0742 0.9072]	$\begin{bmatrix} 1.0667 & -0.0653 & 0.0923 \\ -0.0862 & 1.0688 & 0.0776 \\ -0.0652 & -0.0653 & 0.8927 \end{bmatrix}$
Habit plane	$<\overline{0.6395}\ \overline{0.4793}\ \overline{0.6010}>_{\gamma}$	$<\overline{0.5052}\ 0.5850\ \overline{0.6345}>_{\gamma}$

also are a relatively small fraction, and the change in their population with parent austenite grain refinement is negligible (Fig. 6a). Therefore, the mixed boundaries are not expected to have a significant effect on toughness. On the other hand, the $60^{\circ}/[110]$ twist boundary displays a moderately high energy (765 mJ/m^2) [5] and has the highest population among all intervariant boundaries. In addition, its population decreases with a reduction in parent austenite grain size (Fig. 6a). Since void nucleation is likely to occur at high energy boundaries [54], the martensite produced from fine parent austenite grain structure contains fewer connected high energy boundaries (i.e., $60^{\circ}/[110]$). This in turn slows the coalescence of voids and promotes dimple fracture. In contrast, the martensite formed from coarse grain austenite microstructure includes more connected high energy $60^{\circ}/[110]$ boundaries, accelerating the formation and coalescence of voids and resulting in

Table 3
The calculated equivalent strain associated with Von-Mises criteria for different combinations of variant cluster arrangements in the fine and coarse austenite grained microstructures subjected to martensite transformation.

	Coarse grained microstructure			Fine grained microstructure		
Conditions	min ϵ	variant clustering combinations	possible intervariant boundaries in a packet	min ϵ	variant clustering combinations	possible intervariant boundaries in a packet
2-variants	0.0532	V1V4	$10.5^{\circ}/[0\bar{1}\bar{1}]$	0.0578	V1V4	$10.5^{\circ}/[0\bar{1}\bar{1}]$
					V1V2	$60^{\circ}/[11\bar{1}]$
3-variants	0.0506	V1V3V5	$60^{\circ}/[110]$	0.0509	V1V3V6	$60^{\circ}/[110]$
					V1V2V6	$10.5^{\circ}/[0\bar{1}\bar{1}]$
						$60^{\circ}/[11\bar{1}]$
4-variants	0.0526	V1V2V3V6	$60^{\circ}/[11\bar{1}]$	0.0478	V1V2V3V4	$60^{\circ}/[11\bar{1}]$
			$60^{\circ}/[110]$			$60^{\circ}/[110]$
			$10.5^{\circ}/[0\bar{1}\bar{1}]$			$10.5^{\circ}/[0\bar{1}\bar{1}]$
			$49.5^{\circ}/[110]$			
5-variants	0.0560	V1V2V3V4V6	$60^{\circ}/[11\bar{1}]$	0.0494	V1V2V3V4V6	$60^{\circ}/[11\bar{1}]$
		V1V2V3V5V6	$60^{\circ}/[110]$		V1V2V3V5V6	$60^{\circ}/[110]$
			$10.5^{\circ}/[0\bar{1}\bar{1}]$			$10.5^{\circ}/[0\bar{1}\bar{1}]$
			$49.5^{\circ}/[110]$			$49.5^{\circ}/[110]$
6-variants	0.0560	V1V2V3V4V5V6	$60^{\circ}/[11\bar{1}]$	0.0514	V1V2V3V4V5V6	$60^{\circ}/[11\bar{1}]$
			$60^{\circ}/[110]$			$60^{\circ}/[110]$
			$10.5^{\circ}/[0\bar{1}\bar{1}]$			$10.5^{\circ}/[0\bar{1}\bar{1}]$
			$49.5^{\circ}/[110]$			$49.5^{\circ}/[110]$

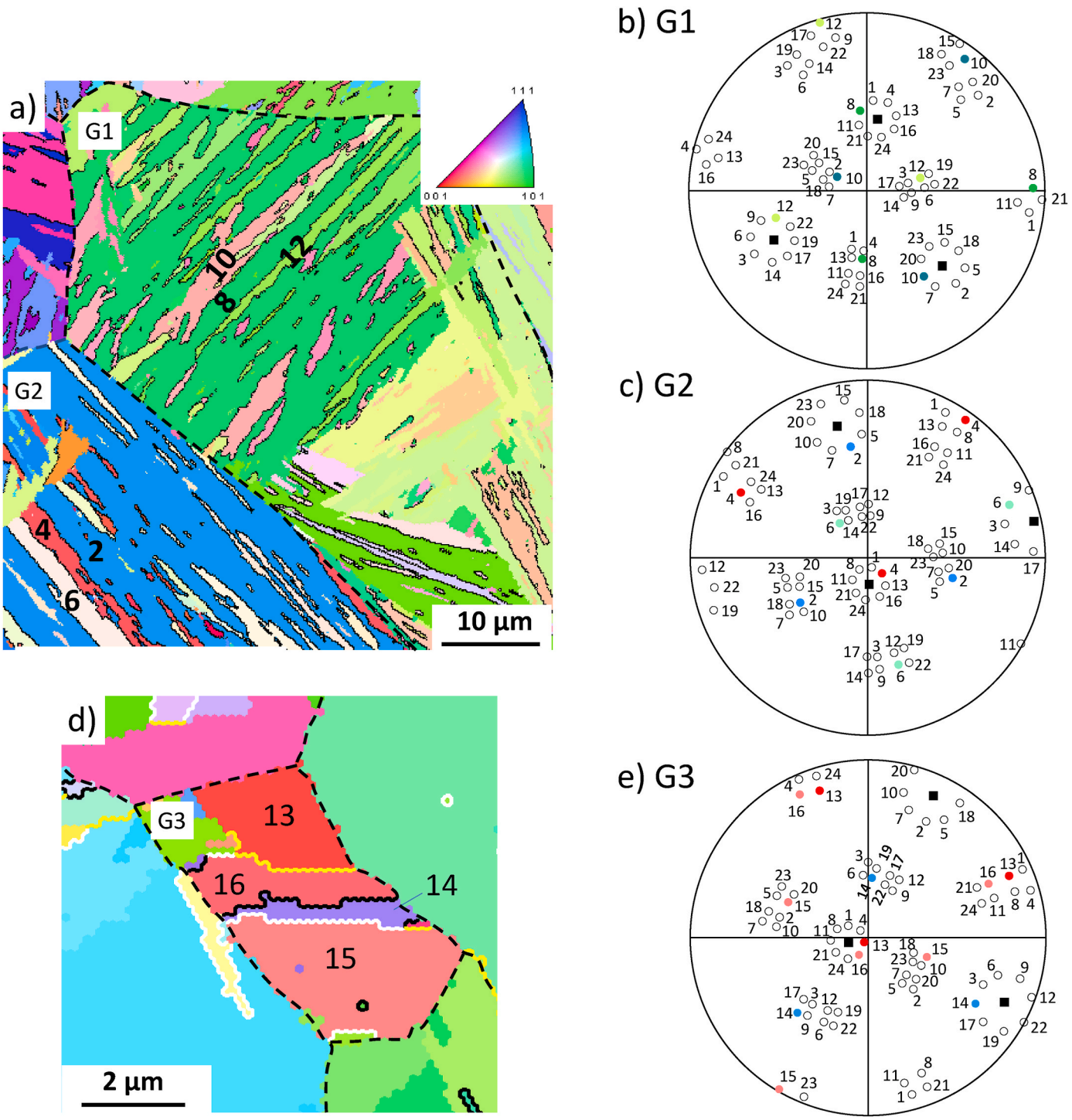

Fig. 10. IPF images of martensite transformed from coarse (a) and fine (d) parent austenite grain structure. b, c and e) Calculated (001) pole figures of 24 K–S theoretical martensite variants (open and colour solid circles) using the orientation of parent austenite (black square) measured using TSL OIM V8 software. The numbers represent variant identification (i.e., 1 through 24) based on the K–S OR as summarised in Table 1. Each colour circle in (b, c and e) corresponds to a given martensite variant labelled in (a) and (d). Black, white, yellow and black dashed lines in (a and d) are 60°/[110], 60°/[111], 10.5°/[110] and parent austenite grain boundaries, respectively. G represents parent austenite grain and the triangle inset in (a) is colour codes referring to the normal direction. (For interpretation of the references to colour in this figure legend, the reader is referred to the Web version of this article.)

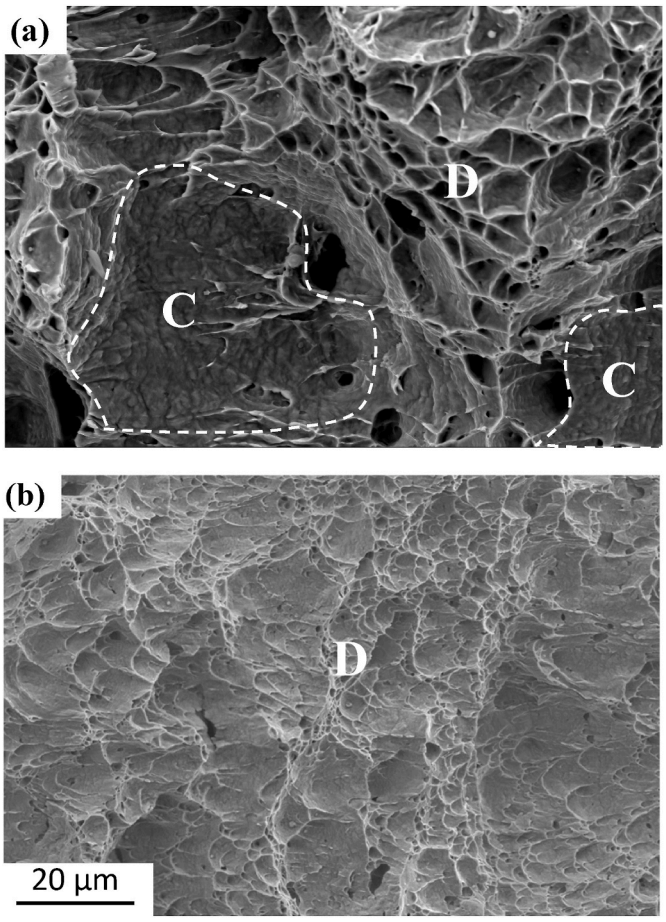

Fig. 11. The fracture surface of the martensite produced from (a) coarse (~84 μm) and (b) fine (~3 μm) parent austenite grain structure. C and D represent cleavage facet, delineated by dashed lines, and dimples, respectively.

partial observation of cleavage fracture even at room temperature (Fig. 11).

These results demonstrate that changes in the austenite parent grain size not only alters the temperature of phase transformations, but importantly, change the boundary network characteristics (i.e., population and connectivity) as a result of variant clustering. This ultimately alters the material performance (i.e., toughness) by weakening the connectivity of high energy boundaries. This is an important finding for enabling the strategic control of the grain boundary network in materials undergoing phase transformation (e.g., steels, Ti, Zr and Co alloys) to target enhanced properties.

5. Conclusion

The current study demonstrated that the parent austenite grain refinement significantly alters the intervariant boundary network population and their connectivity in a lath martensitic steel. This was most pronounced in the population of 60°/[110] intervariant boundaries with twist character, which decreased from ~77 % for a coarse parent austenite grain (i.e., ~84 μm) to ~ 38 % for a fine parent austenite grain size of ~3 μm. The change in the population of intervariant boundaries with parent austenite grain refinement was described using the phenomenological theory of martensite crystallography, which indicated a change in the variant selection mechanism from 3 variant clustering (i.e., $V_1V_3V_5$) in the coarse parent austenite to 4 variant clustering (i.e., $V_1V_2V_3V_4$) in the fine parent austenite grains, to accommodate the strain associated with the martensite transformation. The latter promotes the population of 60°/[111] and 10.5°/[011] intervariant boundaries at the expense of intervariant boundaries with 60°/[110] misorientation. This ultimately influenced the boundary network connectivity in the martensitic microstructure, reducing the connectivity of high energy [110] twist boundaries and increasing the connectivity of the low energy [110] tilt intervariant boundaries. The change in the martensite boundary network enhanced the impact toughness at ambient conditions, since the refinement of the parent austenite grain size reduces the connectivity of high energy boundaries, which defers void coalescence, leading to ductile fracture.

CRediT authorship contribution statement

Ahmad Mirzaei: Methodology, Investigation, Writing – original draft. **Peter D. Hodgson:** Supervision, Writing – review & editing. **Xiang Ma:** Supervision, Writing – review & editing. **Vanessa K. Peterson:** In-situ neutron diffraction experiments, Formal analysis, Writing – review & editing. **Ehsan Farabi:** Formal analysis, Writing – review & editing. **Gregory S. Rohrer:** Formal analysis, Writing – review & editing. **Hossein Beladi:** Supervision, Conceptualization, Methodology, Writing – review & editing.

Declaration of competing interest

The authors declare that they have no known competing financial interests or personal relationships that could have appeared to influence the work reported in this paper.

Data availability

Data will be made available on request.

Acknowledgements

Deakin University's Advanced Characterization Facility is acknowledged for use of the EBSD instruments. The Australian Nuclear Science and Technology Organisation is acknowledged for enabling *in situ* neutron diffraction experiments using Wombat under beamtime proposal P13346. Dr Sitarama Kada is acknowledged for his assistance in analysing the neutron diffraction data.

Appendix A

Instrumental Profile Function: The fundamental parameter approach was used to combine all the contributing effects to the observed instrumental profile function as implemented in the Topas software [28] using data for the NIST $La^{11}B_6$ standard reference material 660b, and as described in Ref. [55] where the instrumental contribution to intensity *Ig* as a function of angle (2θ) was described empirically by a pseudo-Voigt function (Eq. (A1)):

$$I_g(2\theta) = \frac{(1-\eta)}{\pi\sigma}\sqrt{\pi \ln 2}\,exp\left[-\ln 2\left(\frac{2\theta - 2\theta_k}{\sigma}\right)^2\right] + \frac{\eta}{\pi\sigma}\frac{1}{1+\left(\frac{2\theta-2k}{\sigma}\right)^2} \quad \text{Eq. A1}$$

Here η is the fraction of the Lorentzian component, and 2σ is the full width at half maximum (FWHM = 2σ), where 2θ is the reflection position and $2\theta_k$ is the position of the k^{th} reflection.

The coefficients of the Cagliotti equation describing Gaussian broadening U, V, W (Eq. (A2)) and *a*, *b*, *c* of the Lorentzian component (Eq. (A3)) were refined.

$$FWHM^2 = W + V\tan(\theta) + U\,tan^2(\theta) \quad \text{Eq. A2}$$

$$\eta = a + b\theta + c\theta^2 \quad \text{Eq. A3}$$

The lattice parameter of the NIST standard reference material 660b is certified a = 4.15689(8) Å and this was fixed in the refinement and the neutron wavelength and a low-degree Chebyshev polynomial that accounted for the background were refined. The a_i coefficients of the tan(θ) function were refined according to Wilson's suggestion (Eq. (A4)) to account for peak position aberrations.

$$\Delta(2\theta) = a_{-1}\,tan^{-1}(\theta) + a_0 + a_1\tan(\theta) + a_2\,tan^2(\theta) + a_3\,tan^3(\theta) \quad \text{Eq. A4}$$

Parameters were optimized through the minimization of the weighted sum of square difference between the observed ($y_{O,i}$) and calculated intensity ($y_{C,i}$), $w_i(y_{C,i} - y_{O,i})^2$ [56]. The weighted profile R-factor R_{wp} is a discrepancy index scaled by the weighted intensities (Eq. (A5)) [56].

$$R_{wp}^2 = \frac{\sum_i w_i\left(y_{C,i} - y_{O,i}\right)^2}{\sum_i w_i\left(y_{O,i}\right)^2} \quad \text{Eq. A5}$$

The "Chi squared" χ^2 is the average normalized square difference between the calculated and observed values for the number of data points (N) [56], where a value of one represents perfect agreement (Eq. (A6)).

$$\chi^2 = \frac{1}{N}\left(\frac{\sum_i \left(y_{C,i} - y_{O,i}\right)^2}{\sigma^2\left[y_{O,i}\right]}\right. \quad \text{Eq. A6}$$

Fig A1a-b shows the instrumental contribution to the FWHM and Δ(2θ) over the 2θ range of interest. Refined parameters of the neutron instrument as derived from the $La^{11}B_6$ standard are shown in Table A1, where the peak shape contains contributions from the material and the instrument. Fig A1c-d show refinement profiles using neutron powder diffraction data for the $La^{11}B_6$ and the coarse parent austenite grain during cooling at 22 °C. The R_{wp} and χ^2 for the LaB_6 and coarse parent austenite grains at 22 °C are presented in Table A2. *In situ* neutron powder diffraction data were analyzed using sequential refinement to obtain the lattice parameter, with R_{wp} and χ^2 values (Table A2).

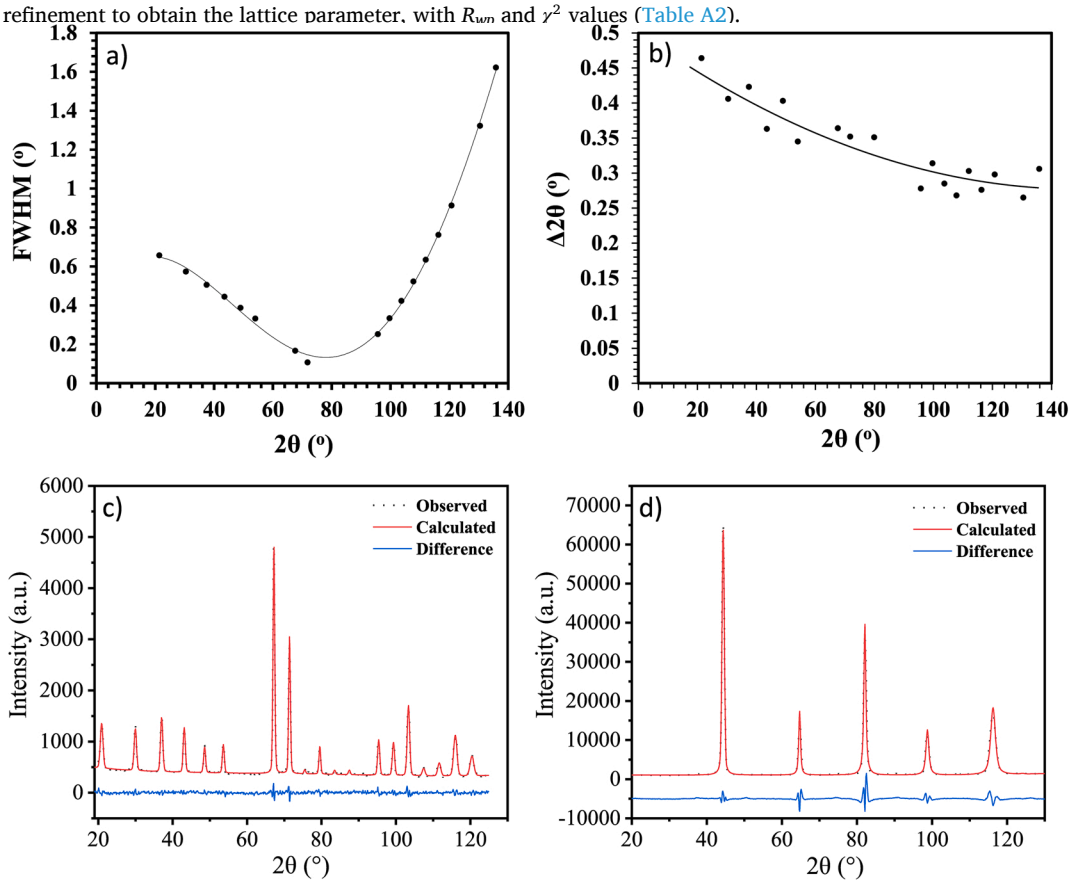

Fig A.1. (a) Full width at half maximum (FWHM) and (b) Δ(2θ) as a function of 2θ as derived from neutron powder diffraction data of the LaB6 standard reference material. The black line through the points is a guide to the eye. Refinement profile using neutron powder diffraction data of (c) La11B6 and (d) the coarse parent austenite grain at 22 °C. Dashed line is related to the observed data. Red line shows the calculated data. Blue line indicates the difference between the observed and calculated data. a.u. represents arbitrary units.

Table A.1
The refined coefficients of the standard expressions for full width at half maximum (FWHM), Lorentzian fraction (η) and Wilson's equation.

U	V	W	a	b	c
1.00860	−1.70655	0.71813	0.00001	−0.00299	0.50049
a_{-1}	**a_0**	**a_1**	**a_2**	**a_3**	—
1.65412	0.4933	−0.0021	6 E−6	8 E−8	—

Table A.2
Weighted profile R-factor and Chi squared for the LaB_6 and coarse parent austenite grains at 22 °C.

	R_{wp}	χ^2
LaB_6	3.47 %	1.27
Coarse parent austenite grains at 22 °C	3.59 %	1.12

Appendix B

Grain boundary plane distribution: The intervariant boundary plane distribution ignoring the misorientation angle displayed a considerable anisotropy, exhibiting the most intense peak at the (101) plane of the transformed martensite originating from the coarse parent austenite grain (i.e., with a diameter ~ 84 μm, Fig. B1a). This indicates that the intervariant boundaries were largely terminated at {101} planes. The maximum population (intensity) was 1.85 multiples of a random distribution (MRD), 85% greater than that expected from a random distribution. The distribution with a minimum intensity terminated at the (001) plane with ~0.4 MRD, whereas the intensity at the (111) plane was ~1 MRD (Fig. B1a). The intervariant boundary distribution was qualitatively similar for different parent austenite grain sizes, revealing the most and least intensity terminated at (101) and (100) planes, respectively. However, the intensity at the (101) plane decreased with parent austenite grain size, reaching ~ 1.5 MRD at a grain size of ~3 μm diameter (Fig. B1d).

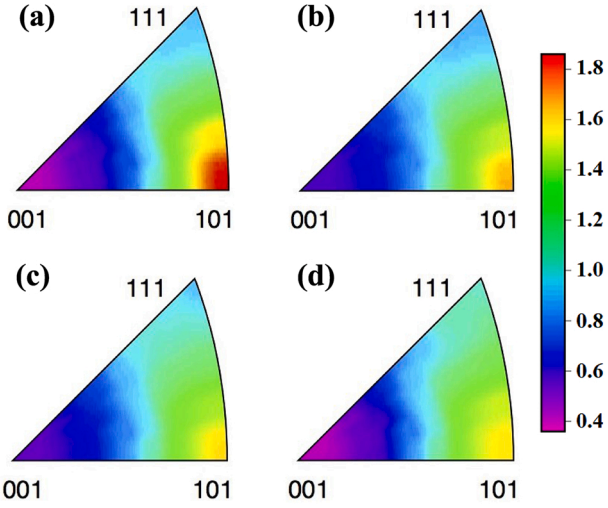

Fig B.1. Intervariant boundary plane character distribution independent of misorientations for the lath martensite microstructure produced from different parent austenite grains; (a) ~ 84 μm, (b) ~ 15 μm, (c) ~ 5 μm, and (d) ~ 3 μm. The colour scale values are in multiples of a random distribution (i.e., MRD).

For boundaries with the misorientation axis of [101], the intervariant boundary distribution largely followed a similar trend to the misorientation of parent austenite grain sizes (Fig. B2). At the 10.5°/[0$\bar{1}$1] misorientation, the grain boundary distribution has weak intensity at the (0-11) plane for a parent austenite grain diameter of 84 μm, with smaller grain sizes leading to intensity at {110} planes up to ~ 6.5 MRD at a grain size of ~3 μm (Fig. B2). At the 49.47°/[011] misorientation, intensity at the {110}||{110} planes (symmetric twist, with the same plane at either side of the boundary) was noted, which decreased with grain refinement, reducing from ~17.8 MRD for a dimeter of ~84 μm to ~ 14 MRD for a diameter ~ 3 μm (Fig. B2). At the higher misorientation angle 60°/[011], the population of this {110}||{110} symmetric twist boundary increased to ~286 MRD for coarse grains (~84 μm diameter) and decreased with grain refinement, reaching ~ 148 MRD at ~ 3 μm (Fig. B2).

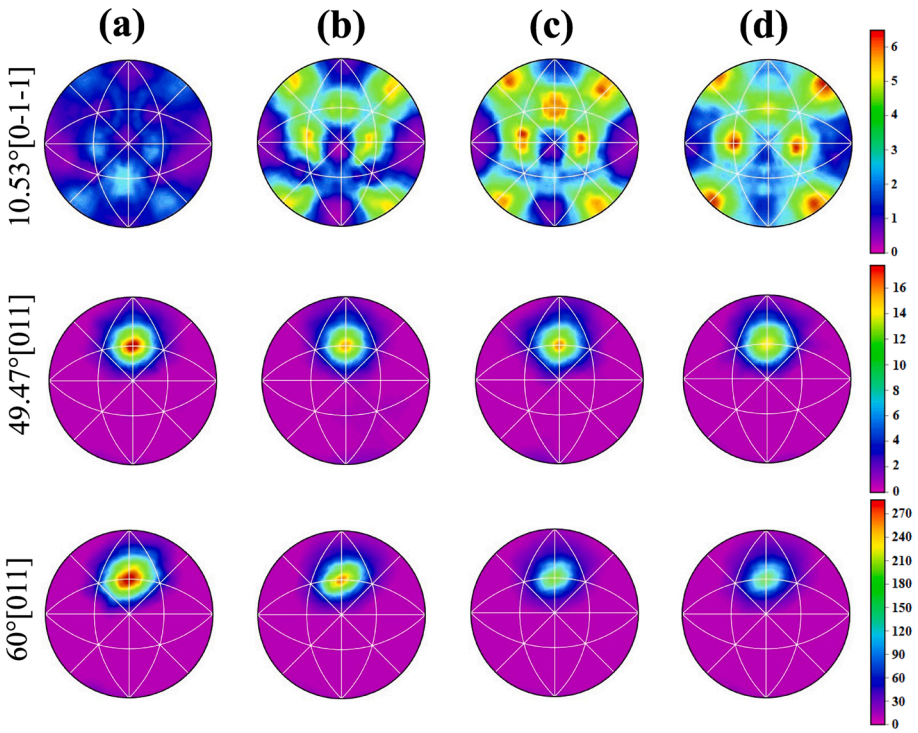

Fig B.2. The effect of parent austenite grain size on the distribution of intervariant boundary plane normals for the boundaries having [110] misorientation axis associated with K-S OR in the lath martensitic microstructure; (a) ~ 84 μm, (b) ~ 15 μm, (c) ~ 5 μm, and (d) ~ 3 μm. The colour scale values are in multiples of a random distribution (i.e., MRD).

For boundaries with the misorientation axis of [111], the distribution was qualitatively similar for different grain sizes for a given lattice misorientation. At the $10.5°/[11\bar{1}]$ misorientation, the intervariant boundary distribution had multimodal intensity at {101} planes for all parent austenite grain sizes (Fig. B3), with grain refinement increasing this from ~2.6 MRD at 84 μm to ~10.7 MRD at the ~3 μm diameter grain size. We note weak intensity at {110} planes where tilt boundaries exist with the zone axis perpendicular to the $[11\bar{1}]$ or $[\bar{1}\bar{1}1]$ directions (Fig. B3). At the $49.5°/[11\bar{1}]$ misorientation, the intensity of tilt boundaries at {110} planes increased with decreasing grain size, from 3.4 MRD at ~84 μm to 9.4 MRD at ~3 μm. At the $60°/[11\bar{1}]$ misorientation, the intervariant distribution preserved this tilt character with ~18 MRD for coarse grains (~84 μm) and increasing to ~ 28 MRD for ~ 3 μm grains (Fig. B3).

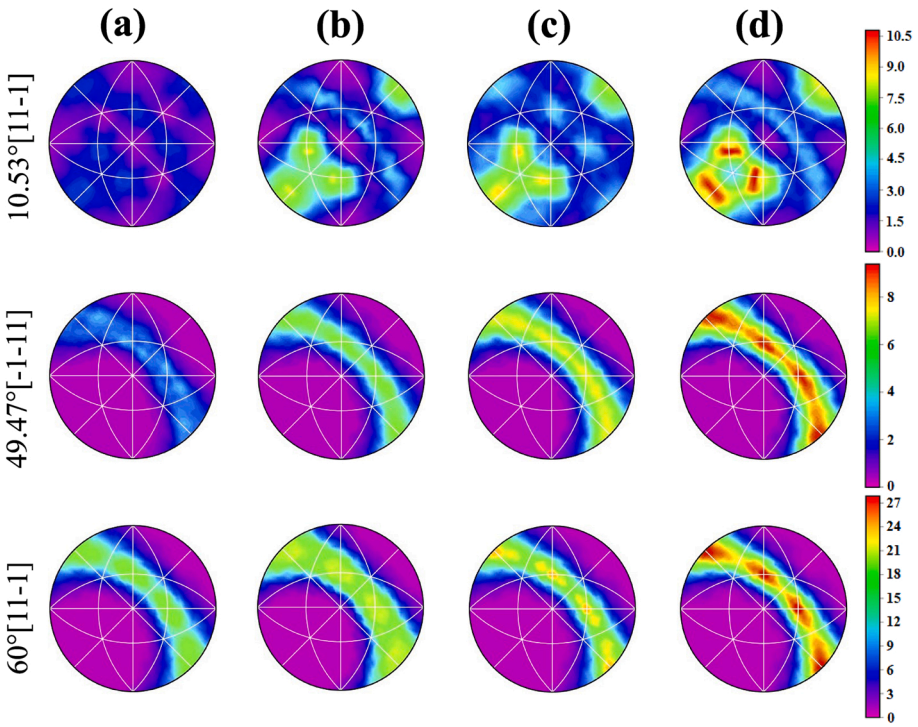

Fig B.3. The effect of parent austenite grain size on the distribution of intervariant boundary plane normals for the boundaries with [111] misorientation axis associated with K-S OR in the lath martensitic microstructure; (a) ~ 84 μm, (b) ~ 15 μm, (c) ~ 5 μm, and (d) ~ 3 μm. The colour scale values are in multiples of a random distribution (i.e., MRD).

For high index misorientations, the intervariant boundary distribution displayed sharp, multimodal intensity near {110} planes (Fig. B4), with intensity below 6 MRD except for 50.5°/[$\bar{7}\bar{5}7$] and 57.2°/[$\bar{3}56$] misorientations that exhibited sharp intensity at the (101) plane. The intensity was changed significantly by parent austenite grain refinement, but differently for different intervariant boundaries. For example, grain refinement led to increased intensity for intervariant boundaries with a 50.5°/[$\bar{7}\bar{5}7$] misorientation, whilst it decreased intensity for 57.2°/[$\bar{3}56$] misorientations. Despite the change of intensity being influenced by parent austenite grain refinement, the distribution of intervariant boundaries remained constant (Fig. B4).

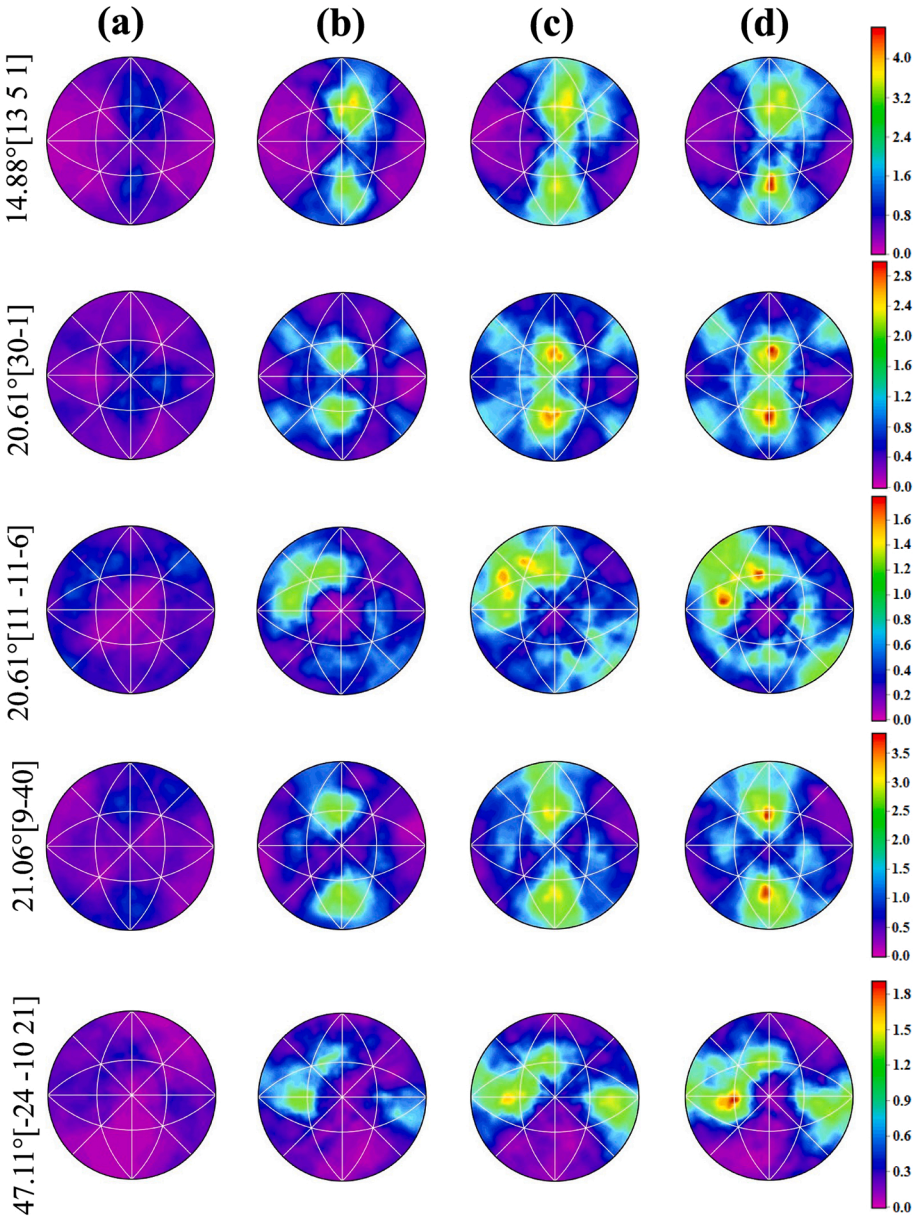

Fig B.4. The effect of parent austenite grain size on the distribution of intervariant boundary plane normals for other intervariant boundaries associated with K-S OR in the lath martensitic microstructure; (a) ~ 84 μm, (b) ~ 15 μm, (c) ~ 5 μm, and (d) ~ 3 μm. The colour scale values are in multiples of a random distribution (i.e., MRD).

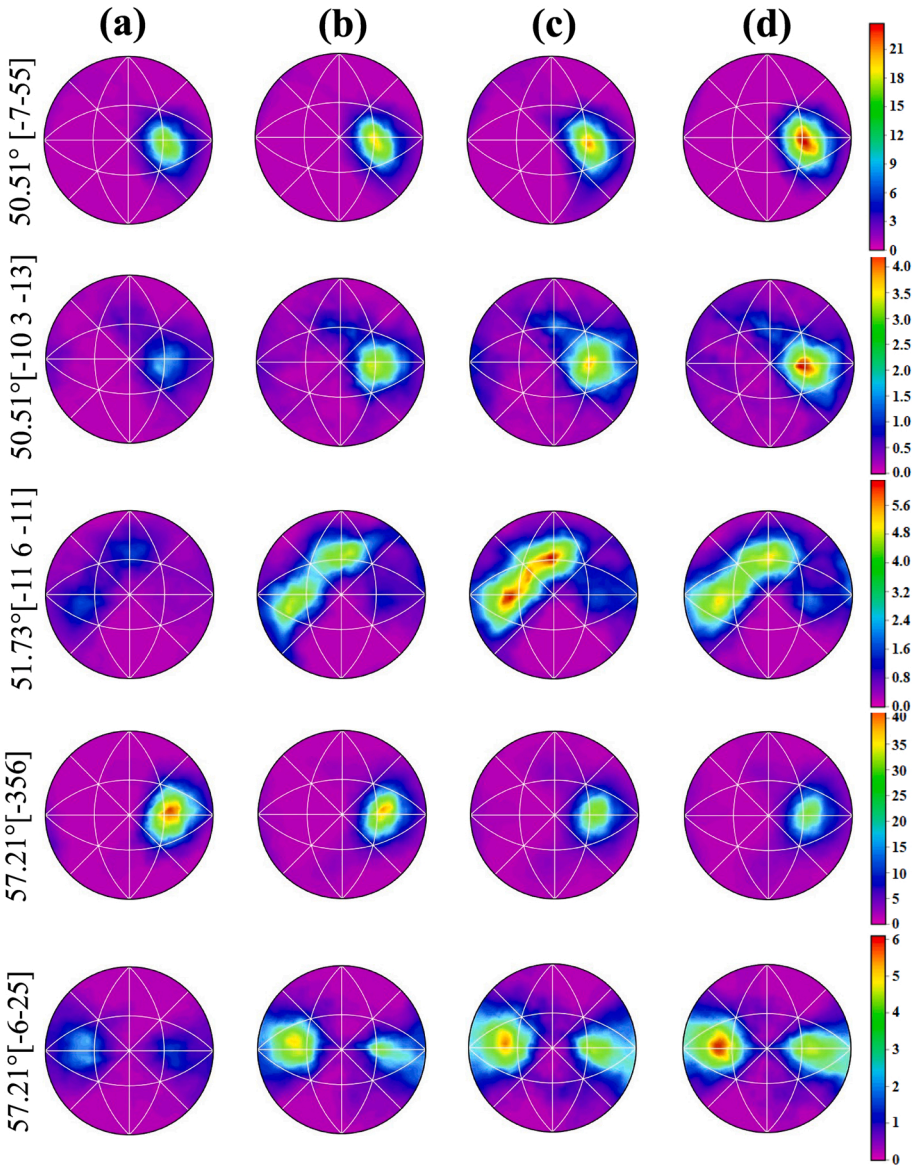

Fig B.4. (*continued*).

Appendix C

Phenomenological theory of martensite crystallography: The shape deformation matrix can be described by Eq. (C1):

$$F = RBS_1S_2 \quad \text{Eq. C1}$$

where F is the shape deformation, R is rigid body rotation, B is Bain strain, and where S_1 and S_2 are lattice invariant shear related to the first (i.e., face centred cubic to body centred tetragonal) and second (i.e., body centred tetragonal to body centred cubic) crystal changes during the austenite to martensite transformation [48]. This formula was used to predict the invariant martensite habit plane (557) in low carbon steels [57]. In this case, the first shear is related to the twining shear within the austenite phase (i.e., $< \bar{1}\bar{1}0 > \gamma(\bar{1}11)\gamma$) followed by the supplementary shear $< \bar{1}\bar{1}0 > \gamma(1\bar{1}2)\gamma$. The predicted invariant habit plane related to the double shear mechanism was compared with the (557) martensite habit plane, which is experimentally observed during martensite transformation [49]. The predicted invariant habit plane for the martensite transformation was 6.86° and 6.16° away from the experimentally observed {557} for the microstructures transformed from coarse and fine parent austenite grains, respectively.

In addition, the strain tensors, T_{ij}, were calculated by identifying the corresponding shape deformation tensors, F_{ij}, of different possible families of martensite variants having the same invariant plane (Eq. C2)

$$T_{ij} = \frac{F_{ij}^t F_{ij} - I}{2} \quad \text{Eq. C2}$$

where F_{ij}^t is the transpose of the shape deformation matrix (F_{ij}) and I the unit matrix.

References

[1] M. Shimada, H. Kokawa, Z. Wang, Y. Sato, I. Karibe, Optimization of grain boundary character distribution for intergranular corrosion resistant 304 stainless steel by twin-induced grain boundary engineering, Acta Mater. 50 (2002) 2331–2341.
[2] C.A. Schuh, M. Kumar, W.E. King, Analysis of grain boundary networks and their evolution during grain boundary engineering, Acta Mater. 51 (2003) 687–700.
[3] K. Aust, U. Erb, G. Palumbo, Interface control for resistance to intergranular cracking, Mater. Sci. Eng., A 176 (1994) 329–334.
[4] H. Kokawa, T. Watanabe, S. Karashima, Sliding behaviour and dislocation structures in aluminium grain boundaries, Philos. Mag. A 44 (1981) 1239–1254.
[5] A. Mirzaei, C.D. Barrett, X. Ma, P.D. Hodgson, H. Beladi, On the propensity of lath martensite intervariant boundaries to hydrogen absorption using molecular statics simulation, Materialia 25 (2022) 101539–101557.
[6] K.N. Solanki, M.A. Tschopp, M.A. Bhatia, N.R. Rhodes, Atomistic investigation of the role of grain boundary structure on hydrogen segregation and embrittlement in α-Fe, Metall. Mater. Trans. 44 (2012) 1365–1375.
[7] M. Kumar, A.J. Schwartz, W.E. King, Microstructural evolution during grain boundary engineering of low to medium stacking fault energy fcc materials, Acta Mater. 50 (2002) 2599–2612.
[8] T. Liu, S. Xia, Q. Bai, B. Zhou, Y. Lu, T. Shoji, Evaluation of grain boundary network and improvement of intergranular cracking resistance in 316L stainless steel after grain boundary engineering, Materials 12 (2019) 242.
[9] S. Kobayashi, S. Tsurekawa, T. Watanabe, A new approach to grain boundary engineering for nanocrystalline materials, Beilstein J. Nanotechnol. 7 (2016) 1829–1849.
[10] V. Randle, Grain boundary engineering: an overview after 25 years, Mater. Sci. Technol. 26 (2013) 253–261.
[11] V. Randle, G. Owen, Mechanisms of grain boundary engineering, Acta Mater. 54 (2006) 1777–1783.
[12] M. Kumar, W.E. King, A.J. Schwartz, Modifications to the microstructural topology in fcc materials through thermomechanical processing, Acta Mater. 48 (2000) 2081–2091.
[13] V. Govindaraj, E. Farabi, S. Kada, P.D. Hodgson, R. P Singh, G.S. Rohrer, H. Beladi, Effect of manganese on the grain boundary network of lath martensite in precipitation hardenable stainless steels, J. Alloys Compd. 886 (2021) 161333–161346.
[14] A. Mirzaei, R. Ghaderi, P.D. Hodgson, X. Ma, G.S. Rohrer, H. Beladi, The influence of parent austenite characteristics on the intervariant boundary network in a lath martensitic steel, J. Mater. Sci. 57 (2022) 8904–8923.
[15] H. Beladi, G.S. Rohrer, The relative grain boundary area and energy distributions in a ferritic steel determined from three-dimensional electron backscatter diffraction maps, Acta Mater. 61 (2013) 1404–1412.
[16] H. Beladi, G.S. Rohrer, A.D. Rollett, V. Tari, P.D. Hodgson, The distribution of intervariant crystallographic planes in a lath martensite using five macroscopic parameters, Acta Mater. 63 (2014) 86–98.
[17] B. Hutchinson, J. Komenda, G.S. Rohrer, H. Beladi, Heat affected zone microstructures and their influence on toughness in two microalloyed HSLA steels, Acta Mater. 97 (2015) 380–391.
[18] H. Beladi, G.S. Rohrer, The role of thermomechanical routes on the distribution of grain boundary and interface plane orientations in transformed microstructures, Metall. Mater. Trans. 48 (2016) 2781–2790.
[19] H. Beladi, V. Tari, I.B. Timokhina, P. Cizek, G.S. Rohrer, A.D. Rollett, P. D. Hodgson, On the crystallographic characteristics of nanobainitic steel, Acta Mater. 127 (2017) 426–437.
[20] K. Ishida, Calculation of the effect of alloying elements on the Ms temperature in steels, J. Alloys Compd. 220 (1995) 126–131.
[21] J. Tian, G. Chen, Y. Xu, Z. Jiang, G. Xu, Comprehensive analysis of the effect of ausforming on the martensite start temperature in a Fe-C-Mn-Si medium-carbon high-strength bainite steel, Metall. Mater. Trans. 50 (2019) 4541–4549.
[22] G. Miyamoto, N. Iwata, N. Takayama, T. Furuhara, Quantitative analysis of variant selection in ausformed lath martensite, Acta Mater. 60 (2012) 1139–1148.
[23] G. Miyamoto, N. Iwata, N. Takayama, T. Furuhara, Variant selection of lath martensite and bainite transformation in low carbon steel by ausforming, J. Alloys Compd. 577 (2013) S528–S532.
[24] C. Celada-Casero, J. Sietsma, M.J. Santofimia, The role of the austenite grain size in the martensitic transformation in low carbon steels, Mater. Des. 167 (2019) 107625–107634.
[25] S. Van Bohemen, L. Morsdorf, Predicting the Ms temperature of steels with a thermodynamic based model including the effect of the prior austenite grain size, Acta Mater. 125 (2017) 401–415.
[26] T. Hanamura, S. Torizuka, S. Tamura, S. Enokida, H. Takechi, Effect of austenite grain size on transformation behavior, microstructure and mechanical properties of 0.1C–5Mn martensitic steel, ISIJ Int. 53 (2013) 2218–2225.
[27] ASTM A1033-04, Standard Practice for Quantitative Measurement and Reporting of Hypoeutectoid Carbon and Low-Alloy Steel Phase Transformations, ASTM International, est Conshohocken, PA, USA, 2004.
[28] A.J. Studer, M.E. Hagen, T.J. Noakes, Wombat: the high-intensity powder diffractometer at the OPAL reactor, Phys. B Condens. Matter 385–386 (2006) 1013–1015.
[29] http://www.topas.imst.de/Topas/en/downloads.php.
[30] G.S. Rohrer, H.M. Miller, Topological characteristics of plane sections of polycrystals, Acta Mater. 58 (10) (2010) 3805–3814.
[31] F.J. Parker, R.W. Rice, Correlation between grain size and thermal expansion for aluminum titanate materials, J. Am. Ceram. Soc. 72 (1989) 2364–2366.
[32] A. Ahadi, Y. Matsushita, T. Sawaguchi, Q.P. Sun, K. Tsuchiya, Origin of zero and negative thermal expansion in severly-deformed superplastic NiTi alloy, Acta Mater. 124 (2017) 79–92.
[33] T. Furuhara, K. Kikumoto, H. Saito, T. Sekine, T. Ogawa, S. Morito, T. Maki, Phase transformation from fine-grained austenite, ISIJ Int. 48 (2008) 1038–1045.
[34] Z. Nasiri, S. Ghaemifar, M. Naghizadeh, H. Mirzadeh, Thermal mechanisms of grain refinement in steels: a Review, Met. Mater. Int. (2020) 2078–2094.
[35] A.B. Cota, C.A.M. Lacerda, F.L.G. Oliveira, F.A. Machado, d. Silva Araújo, Effect of the austenitizing temperature on the kinetics of ferritic grain growth under continuous cooling of a Nb microalloyed steel, Scripta Mater. 51 (7) (2004) 721–725.
[36] V. Randle, Refined approaches to the use of the coincidence site lattice, JOM (J. Occup. Med.) 50 (1998) 56–59.
[37] V. Randle, Mechanism of twinning-induced grain boundary engineering in low stacking-fault energy materials, Acta Mater. 47 (1999) 4187–4196.
[38] N. Haghdadi, P. Cizek, P.D. Hodgson, V. Tari, G.S. Rohrer, H. Beladi, Effect of ferrite-to-austenite phase transformation path on the interface crystallographic character distributions in a duplex stainless steel, Acta Mater. 145 (2018) 196–209.
[39] H. Beladi, V. Tari, A.D. Rollett, G.S. Rohrer, The influence of γ-fibre texture on grain boundary character distribution of an IF-steel, Scripta Mater. 222 (2023), 115042.
[40] H. Beladi, Q. Chao, V. Tari, A.D. Rollett, G.S. Rohrer, The influence of processing and texture on the grain boundary character distribution of an austenitic Ni-30Fe alloy, Mater. Char. 197 (2023), 112708.
[41] B.R. Kumar, S.K. Das, B. Mahato, A. Das, S. Ghosh Chowdhury, Effect of large strains on grain boundary character distribution in AISI 304L austenitic stainless steel, Mater. Sci. Eng., A 454–455 (2007) 239–244.

[42] M. Michiuchi, H. Kokawa, Z.J. Wang, Y.S. Sato, K. Sakai, Twin-induced grain boundary engineering for 316 austenitic stainless steel, Acta Mater. 54 (2006) 5179–5184.
[43] A.J. Schwartz, W.E. King, M. Kumar, Influence of processing method on the network of grain boundaries, Scripta Mater. 54 (2006) 963–968.
[44] T. Liu, S. Xia, H. li, B. Zhou, Q. Bai, C. Su, Z. Cai, Effect of initial grain sizes on the grain boundary network during grain boundary engineering in Alloy 690, J. Mater. Res. 28 (2013) 1165–1176.
[45] T. Tomida, Variant selection mechanism by elastic anisotropy and double K-S relation for transformation texture in steel; difference between martensite and ferrite, Acta Mater. 146 (2018) 25–41.
[46] T. Tomida, M. Wakita, M. Yasuyama, S. Sugaya, Y. Tomota, S.C. Vogel, Memory effects of transformation textures in steel and its prediction by the double Kurdjumov-Sachs relation, Acta Mater. 61 (2013) 2828–2839.
[47] F. Archie, S. Zaefferer, On variant selection at the prior austenite grain boundaries in lath martensite and relevant micro-mechanical implications, Mater. Sci. Eng., A 731 (2018) 539–550.
[48] H.K.D.H. Bhadeshia, Worked examples in the geometry of crystals, in: second ed. Acta Crystallographica Section A, vol. 57, Institute of Materials, London, 2006, p. 478.
[49] A.A. Zisman, Unique properties of habit plane (557) in origination of lath martensite, Mater. Lett. 275 (2020) 128140–128143.
[50] P.M. Kelly, Crystallography of lath martensite in steels, Mater. Trans., JIM 33 (1992) 235–242.
[51] T. Watanabe, S. Tsurekawa, Toughening of brittle materials by grain boundary engineering, Mater. Sci. Eng., A 387–389 (2004) 447–455.
[52] S. Plimpton, Fast parallel algorithms for short-range molecular dynamics, J. Comput. Phys. 117 (1) (1995) 1–19.
[53] M. Wen, A new interatomic potential describing Fe-H and H-H interactions in bcc iron, Comput. Mater. Sci. 197 (2021) 110640–110646.
[54] J. Kang, C. Wang, G.D. Wang, Microstructural characteristics and impact fracture behavior of a high-strength low-alloy steel treated by intercritical heat treatment, Mater. Sci. Eng., A 553 (2012) 96–104.
[55] P. Scardi, Diffraction line profiles in the Rietveld method, Cryst. Growth Des. 20 (2020) 6903–6916.
[56] B.H. Toby, R factors in Rietveld analysis: how good is good enough? Powder Diffr. 21 (2012) 67–70.
[57] S. Morito, H. Tanaka, R. Konishi, T. Furuhara, T. Maki, The morphology and crystallography of lath martensite in Fe-C alloys, Acta Mater. 51 (2003) 1789–1799.